scientific reports

OPEN

Tumor-specific PET tracer imaging and contrast-enhanced Mri based tumor volume differences inspection of glioblastoma patients

Irshad Ahmed Abbasi[1][✉], Mohammed Alshehri[2] & Yahya AlQahtani[3]

Despite advancements in treatment strategies, glioblastoma, also known as GBM, remains an exceptionally aggressive primary brain tumor with a grim prognosis. Despite innovations in treatment strategies, GBM continues to pose significant challenges. The assessment of GBM mainly depends on neuroimaging methods, with contrast-enhanced magnetic resonance imaging (MRI) being the widely accepted standard. In recent years, positron emission tomography (PET) has emerged as a supplementary imaging modality offering insights into the biological behavior and aggressiveness of GBM tumors. PET, often referred to as PET, complements MRI in the diagnostic process of GBM. The objective of this study was to explore the potential advantages of combining PET and MRI in diagnosing GBM. Twenty-two patients diagnosed with GBM underwent four 18 F-fluorothymidine (FLT)-PET/MRI examinations before and during treatment. Advanced image analysis methods, including MATLAB and the imlook4d analysis platform, were employed. These methods encompassed adaptive threshold algorithms, batch processing pipelines, and image attribute extraction algorithms. MRI evaluations revealed significant variations in tumor response to radiation therapy among patients with long-term and short-term survival rates, as determined by the study findings ($p < 0.04$). Furthermore, PET measurements, including maximum standardized uptake value (SUVmax), PET tumor volume, and total lesion activity (TLA), showed trends toward statistical significance; however, the differences did not reach conventional significance thresholds. These results underscore the need for further research into the therapeutic efficacy of PET parameters in managing this aggressive brain tumor. The findings of this study highlight the potential of fusion imaging using PET and MRI as an effective diagnostic technique for glioblastoma multiforme (GBM) and emphasize the importance of ongoing research in this area to improve patient outcomes.

Keywords Positron emission tomography, Magnetic resonance imaging, Glioblastoma, Tumor, Medical image processing, 18F-Fluorothymidine

GBM, the more severe variant of glioma, is predominantly observed in the adult population. An estimated sixty to seventy% of all gliomas are denoted by this malignancy[1]. Patients who have received a diagnosis of GBM are met with an alarmingly brief median survival span of 10–12 months[2]. Despite substantial advancements in therapeutic modalities including radiation, chemotherapy, surgical resection, and GBM, the aggressive characteristics of this malignancy persist[3]. Rapid progression and invasive tendencies characterize this aggressive nature, which almost invariably leads to a recurrence[4]. In 2023, approximately 500 cases of GBM were identified in Sweden. The incidence rate for males was 5.15 cases per 100,000 residents, compared to 3.87 cases per 100,000 residents for females[5]. Glioblastoma multiforme (GBM) is the most common and aggressive primary brain tumor in adults worldwide. Globally, GBM accounts for approximately 15% of all brain tumors and around 45–50% of malignant primary brain tumors. The annual incidence rate is estimated at 3.2 cases per 100,000 population, with higher prevalence observed in older adults and males. However, the advent of 5-aminolevulinic acid fluorescence microsurgery has significantly transformed the array of surgical interventions accessible for GBM, enabling the execution of radiological bulk complete tumor excision[6]. After undergoing surgical intervention, combination

[1]Department of Computer Science and Artificial Intelligence, College of Computing and Information Technology, University of Bisha, Bisha 67714, Saudi Arabia. [2]Department of Computer Science, King Khalid University, Abha 61421, Saudi Arabia. [3]Department of Informatics and Computer Systems, King Khalid University, Abha 61421, Saudi Arabia. ✉email: aabasy@ub.edu.sa

1

therapy is a customary component of the postoperative regimen[7]. This therapy consists of concurrent and adjuvant chemotherapy utilizing temozolomide in addition to radiotherapy administered at dosages of up to 60 Gy[8]. Despite the implementation of concerted efforts, GBM remains a devastating disease with an unfavorable prognosis[9]. Given the challenges in accurately assessing GBM, improving imaging techniques for better tumor delineation and treatment planning remains a critical focus[10]. Recent studies have underscored the advantages of integrating PET and MRI in the domain of GBM monitoring and treatment[11]. The fusion imaging technique of PET/MRI provides an excellent opportunity to obtain comprehensive insights into the tumor's aggressiveness and biological behavior, thereby enhancing therapeutic decision-making and prognostication accuracy[12]. The aforementioned findings underscore the potential of PET/MRI as a crucial instrument in the identification and treatment of GBM[13]. Additionally, they emphasize the need for additional research endeavors in order to fully comprehend the clinical significance of this method.

The present study focuses on the investigation of GBM diagnosis and management. The study specifically examines the potential advantages that may arise from the the combination of MRI and PET in the context of GBM diagnosis and treatment. Present diagnostic protocols are dependent on contrast-enhanced MRI. Although this technique proves beneficial, it is not without its limitations when it comes to accurately identifying recurrent tumors, determining precise tumor volume, and differentiating between treatment-induced effects and progressive tumor growth[14]. In contrast, PET illuminates the biological characteristics of GBM through the use of non-invasive imaging techniques. Additionally, it can support the categorization of tumor cells non-invasively, aid in the development of surgical plans, and assess the efficacy of radiation therapy[15].

The potential benefits of integrating PET and MRI data via multimodal imaging techniques in the diagnosis of GBM are considerable[16]. By implementing this approach, it would be feasible to assess treatment response early, forecast prognosis, and optimize treatment regimens to mitigate the risk of ineffectual interventions and potential adverse events[17]. Further research is required to fully comprehend the clinical effectiveness of this integrated imaging method. Additional research is necessary to validate the prospective advantages of PET/MRI in the diagnosis and treatment of GBM. The purpose of this specific investigation is to ascertain whether or not FLT-PET/MR imaging can be utilized to assess early treatment response and forecast outcomes for newly diagnosed patients with glioblastoma multiforme. A primary aim is to establish accurate algorithms that can accurately assess the distribution of tumors and facilitate the comparison between contrast-enhanced MRI images and FLT-PET images. Furthermore, a comparative analysis of the two forms of imaging is also worth considering. Upon comparing long-term survivors to short-term survivors, the study's results reveal that long-term survivors exhibited superior treatment responses as evaluated by both MRI and PET. PET also demonstrated an increased capacity for prediction in determining progression-free survival. In terms of forecasting a patient's overall survival and response to radiochemotherapy, the integration of PET and MRI data exhibits potential. With the exception of the study's sample size, further research involving a more extensive cohort is necessary. The robust results suggest that FLT-PET/MRI imaging may serve as a valuable tool in the monitoring of treatment efficacy and management of glioblastoma multiforme[8].

This study makes several significant contributions to the field of GBM diagnosis and treatment, particularly in the integration of advanced imaging modalities. The key contributions are as follows:

- The study introduces an exclusive dataset comprising 207 high-quality DICOM images collected using a state-of-the-art GE SIGNA PET/MRI scanner. This dataset includes meticulously processed attenuation-corrected PET images and gadolinium-enhanced T1-weighted MRI images, offering a valuable resource for future research.
- By integrating FLT-PET and gadolinium-enhanced MRI data, this study enhances the diagnostic accuracy and monitoring of GBM. The preprocessing techniques, including PET matrix resampling and voxel normalization to standardized uptake values (SUVs), ensure the seamless alignment and quantification of imaging data, enabling precise tumor evaluation.
- The study critically evaluates the limitations of widely used imaging agents, such as FLT and Gd, highlighting their challenges in differentiating tumor tissue from treatment-induced changes and their specificity in detecting malignant neoplasms. These insights pave the way for further research into alternative imaging techniques.
- The study underscores the importance of follow-up imaging within 48 h of surgery, shedding light on the complexities of interpreting post-surgical contrast enhancement due to radiotherapy or surgical interventions.
- This study demonstrates the effectiveness of combining FLT-PET and MRI for assessing treatment response, forecasting progression-free survival, and predicting overall survival. This integration establishes a robust framework for improving therapeutic decision-making in GBM management.
- The methodologies and insights presented in this study set the stage for further investigations into innovative imaging strategies for GBM. The work encourages exploring advanced algorithms and larger datasets to refine imaging techniques and improve patient outcomes.

This article begins with an Introduction, outlining the challenges of GBM diagnosis and treatment and highlighting the potential of PET/MRI integration. The Literature Review explores current imaging modalities, advances in multimodal imaging, and research gaps justifying this study. The Methodology describes a dataset of 207 FLT-PET and gadolinium-enhanced MRI images from IRNUM, Pakistan, and details preprocessing, analysis using MATLAB and imlook4d, and evaluation metrics. The Results and Discussion present findings on the predictive value of PET/MRI in assessing treatment response and prognosis while addressing clinical implications. The article concludes with limitations and future research directions, focusing on alternative imaging methods and larger datasets.

Literature review

Okaili et al.[18] addressed the criteria for distinguishing intra-axial brain masses and evaluating the accuracy of MRI images. The institutional review board approved the protocol, which included diffusion-weighted MRI, perfusion MRI, proton MRI spectroscopy, conventional MRI, and the classification of intra-axial masses into three categories: high-grade primary tumors, metastatic tumors, and low-grade primary tumors. The accuracy of the system was evaluated utilizing a Bayesian statistical methodology. Anila et al.[19] utilized the concept of multi-resolution and noise reduction in order to detect the anomalous brain activity. Approximations based on curvelets and countrelets formed the basis of the multi-resolution. The counterlet method has been shown to be more effective at detecting abnormalities in the brain. A comprehensive examination of the diverse techniques employed in segmenting MRI images and identifying brain tumors was addressed by Balafar et al.[20]. The segmentation techniques influence the accuracy of tumor detection. Anatomical deviations, Markov's random model, watershed algorithm, self-organizing maps, atlas-based segmentation, and a multiregion-based approach were among the topics discussed. Combining parallelization and the atlas-based approach is suggested as a means to improve brain segmentation. Chaudhary et al.[21] examined the concept of application of clustering for image segmentation, while the detection of brain tumors is achieved through the utilization of a support vector machine (SVM). The classifiers successfully identified the seven features, with SVM achieving an accuracy of 94.6%. As highlighted by Gholipour et al.[22], automated functional localization and functional brain imaging are crucial for achieving temporal and higher resolution insights into brain malignancies. The utilization of functional maps facilitates the identification of dementia, a condition in which cancer patients and healthy individuals may exhibit substantial differences. It will lead to interpretations and deductions that are rational. The time-consuming nature of tumor segmentation from MRI data has been recognized by medical personnel; thus, Ratan et al.[23] investigated numerous techniques designed to achieve this objective. A variety of techniques were emphasized in the presentation, such as intensity, level set methods, watershed algorithms, atlas-guided techniques, morphological operations, fuzzy C-means clustering, fuzzy neural networks, region-based clustering, classification methods, knowledge-based approaches, edge detection, probabilistic models, fusion techniques, and SVM. It was suggested that the most effective approach for brain tumor detection could be achieved by integrating thresholding with SVM or Basian methods. By calculating the tumor's area and conducting symmetry analysis, Ratan et al.[24] proposed a method for identifying malignancies from MRI images. They utilize morphological operations, thresholding, and median filters to detect tumors. For semi-automatic hepatic tumor segmentation, Li et al.[25] integrated prior tumor, image gradient, and regional competition data using a unified level set technique. The method was applied directly to contrast-enhanced computed tomography (CT) images, followed by the use of unsupervised fuzzy clustering to generate the probability distribution of hepatic tumors. In their study, Thapaliya et al.[26] employed the level set approach and an automated selection of local statistics to segment brain tumors. The threshold parameters were determined automatically modified and rationalized for each MRI image. Goel et al.[27] discussed the level set approach and watershed algorithm utilized in the segmentation of brain tumor areas from MRI images. To assess the efficacy and response time of MATLAB, a comparative analysis is undertaken. The level set approach, in contrast, has produced a favorable response to Otsu's thresholding technique. According to Mustaqeem et al.[28], brain malignancies can be detected using morphological operators, threshold segmentation, and watershed segmentation. By applying these techniques to scanned MRI images, they successfully simulated human brain tissue. Patil et al.[29] applied morphological operators and the watershed method to differentiate malignancies in brain MRI images. These methods involved the use of morphological operators, area segmentation, and noise reduction techniques on the scanned MRI images. Remya et al.[30] utilized the Fuzzy-C means method in order to eliminate noise from MRI images. The procedure thoroughly examines the identification of the cerebrum tumor. The method of Otsu was implemented to segment images. The fuzzy-C means method yielded favorable results, even when the patient took into account the presence of the tumor, as stated by the authors. Sain et al.[31] delineated the anatomical features of the human brain and proposed a brain tumor detection algorithm predicated on Otsu's segmentation method. Amin et al.[32] fused images using DWT to provide comprehensive information on the MRI regions associated with brain lesions. The global thresholding technique is utilized to segment tumors subsequent to the elimination of noise through the implementation of the partial diffusion filter. Khode et al.[33] utilized DWT for the purpose of discovering brain lesions. In numerous circumstances, MRI can provide a comprehensive imaging analysis of the human body, making it a highly practical method. Utilizing the MRI scans, the tumor was segmented for the examination. Kumar et al.[34] introduced the utilization of DWT for the purpose of image segmentation. Additionally, they distinguished the circular, inclined, and vertical areas. Using the HAAR DWT method, the image was partitioned into four sub-bands denoted as "LL," "LH," "HL," and "HH," each with a coefficient of + 1 or -1. Shree et al.[35] note that identifying, detecting, and accurately segmenting the location of a brain tumor in MRI images is a complex and time-intensive task. Due to the presence of numerous modalities and noise in MRI images, the system must rapidly analyze and transform data. By employing DWT for image segmentation and morphological filters to reduce noise, the system's efficacy was enhanced. Singh and colleagues[36] proposed the utilization of DWT and DCT are employed in image processing tasks. In order to compress and watermark images, they utilized the DWT and DCT.

Attention mechanisms have emerged as a powerful tool in medical image segmentation, enabling models to focus on critical regions of interest within an image[37]. Recent studies have incorporated self-attention and multi-head attention layers within deep neural networks to improve segmentation accuracy, particularly for complex medical imaging tasks. These mechanisms enhance the interpretability and precision of segmentation by dynamically weighting image features based on their importance.

Encoder-decoder architectures, such as U-Net and its variants, remain a cornerstone of medical image segmentation[38]. These architectures employ symmetric skip connections that preserve spatial information and

ensure accurate localization of features. Enhanced versions, such as Attention U-Net, integrate attention gates to further refine the segmentation process by suppressing irrelevant regions and emphasizing target areas.

Transformers, initially designed for natural language processing, have been adapted for image segmentation tasks. Vision Transformers (ViTs) are particularly effective in capturing long-range dependencies within medical images[39], offering superior segmentation results compared to traditional convolutional models. By leveraging global self-attention mechanisms, ViTs enable more precise delineation of anatomical structures and pathological regions.

Deep learning techniques, including Convolutional Neural Networks (CNNs), have revolutionized the field of medical image segmentation[40]. Moeskops et al. applied CNNs to segment MRI brain images into distinct tissue categories across diverse datasets, achieving high precision for individuals of varying age groups. Similarly, Pereira et al. designed a deep CNN architecture with minimal kernels (3×3) for brain MRI segmentation, validated using the BRATS-2013 and BRATS-2015 datasets.

Methodology
Datasets
We have compiled a comprehensive and well-structured dataset through the meticulous collection of image data obtained from the prestigious Institute of Radiotherapy and Nuclear Medicine (IRNUM) in Khyber Pakhtunkhwa, Pakistan. Utilizing the advanced and state-of-the-art GE SIGNA PET/MRI scanner, we acquired a comprehensive set of imaging data, comprising accurately captured and processed attenuation-corrected and reconstructed PET images, along with the invaluable gadolinium-enhanced T1-weighted images.

Our dataset encompasses a total of 207 meticulously selected digital imaging and communications in medicine (DICOM) images, forming the foundation for our rigorous image analysis endeavors. This intricate analysis process was meticulously carried out employing industry-standard tools such as MATLAB and the renowned imlook4d, ensuring the highest degree of precision and accuracy throughout the analytical pipeline.

To ensure a harmonious and coherent integration of the PET and T1-weighted images, a crucial preprocessing step involved the meticulous resampling of the PET matrix, precisely aligning it with the exact slice positions of the T1-weighted images. Subsequently, to facilitate standardized and consistent quantitative analysis, a vital step encompassed the normalization of voxel values to standardized uptake values (SUV), ensuring the establishment of a common metric for accurate assessment and comparison. This normalization process followed the formulation provided by Eq. (3), seamlessly integrating the essential mathematical framework into our analytical workflow.

While FLT and Gd have emerged as widely utilized PET tracer and MRI contrast agent, respectively, for the assessment of brain tumors, it is imperative to acknowledge their inherent limitations. Notably, FLT uptake, although serving as an indicator of cellular activity, lacks specificity when discerning malignant neoplasms, as it can be influenced by factors such as increased permeability resulting from blood-brain barrier disruption, which may also manifest in bone marrow and treatment-induced alterations. On the other hand, Gd, despite its established utility, necessitates careful chelation to ensure safe utilization in MRI due to its inherent toxicity. Moreover, differentiating between tumor tissues and surgical invasions poses a formidable challenge.

In this study, we employed 18 F-fluorothymidine (18 F-FLT) as the PET tracer for imaging glioblastoma multiforme (GBM). 18 F-FLT is a thymidine analog that functions as a proliferation-specific radiotracer by targeting thymidine kinase-1 (TK1), an enzyme upregulated during DNA synthesis in actively dividing cells. FLT is phosphorylated intracellularly and retained within proliferating cells, making it a valuable marker for assessing tumor cell proliferation. This characteristic renders 18 F-FLT a "tumor-specific" tracer, particularly advantageous for identifying active tumor regions beyond the contrast-enhancing zones visible on MRI. Unlike amino acid tracers such as 18 F-FET or 11 C-methionine, which accumulate based on increased transport in tumor cells, FLT provides more direct insight into mitotic activity, thereby offering complementary biological information that enhances the delineation of aggressive tumor subregions and contributes to more informed treatment planning and monitoring.

All imaging data were acquired using the GE SIGNA PET/MRI hybrid scanner, which integrates simultaneous PET and MRI acquisition. This system enabled exact co-registration between PET and MR images by capturing both modalities during a single imaging session without repositioning the patient. Consequently, issues related to alignment or time-lag variability between modalities were inherently minimized. The MRI component involved contrast-enhanced T1-weighted imaging, using gadolinium-based contrast agents to visualize the enhancing tumor core. Simultaneously, 18 F-FLT PET images were acquired to assess tumor proliferation. For PET imaging, attenuation correction was automatically performed using MRI-based correction algorithms native to the hybrid scanner. No separate image smoothing was applied during acquisition.

To evaluate surgical efficacy and determine the presence of any residual tumor tissue, the integration of follow-up MRI with contrast enhancement within a 48-hour timeframe following surgery assumes paramount importance. Such subsequent examinations often reveal contrast enhancement attributed to surgical intervention and the effects of radiotherapy. As shown in Fig. 1, pre-surgical FLT-PET/MRI brain imaging highlights glioblastoma contrast enhancement on Gd-enhanced MRI and FLT-PET activity concentration. The PET image was normalized to create a Gd-enhanced T1-weighted MRI matrix. While FLT PET and contrast-enhanced MRI images of GBM offer invaluable insights and information, it is crucial to consider and account for the aforementioned limitations. Therefore, exploring alternative imaging methodologies and approaches is imperative to enhance the accuracy of diagnosis and improve the efficacy of treatment monitoring, ultimately augmenting patient outcomes and prognoses.

The normalization process followed the formulation provided by Eq. (3), which can be expressed as:
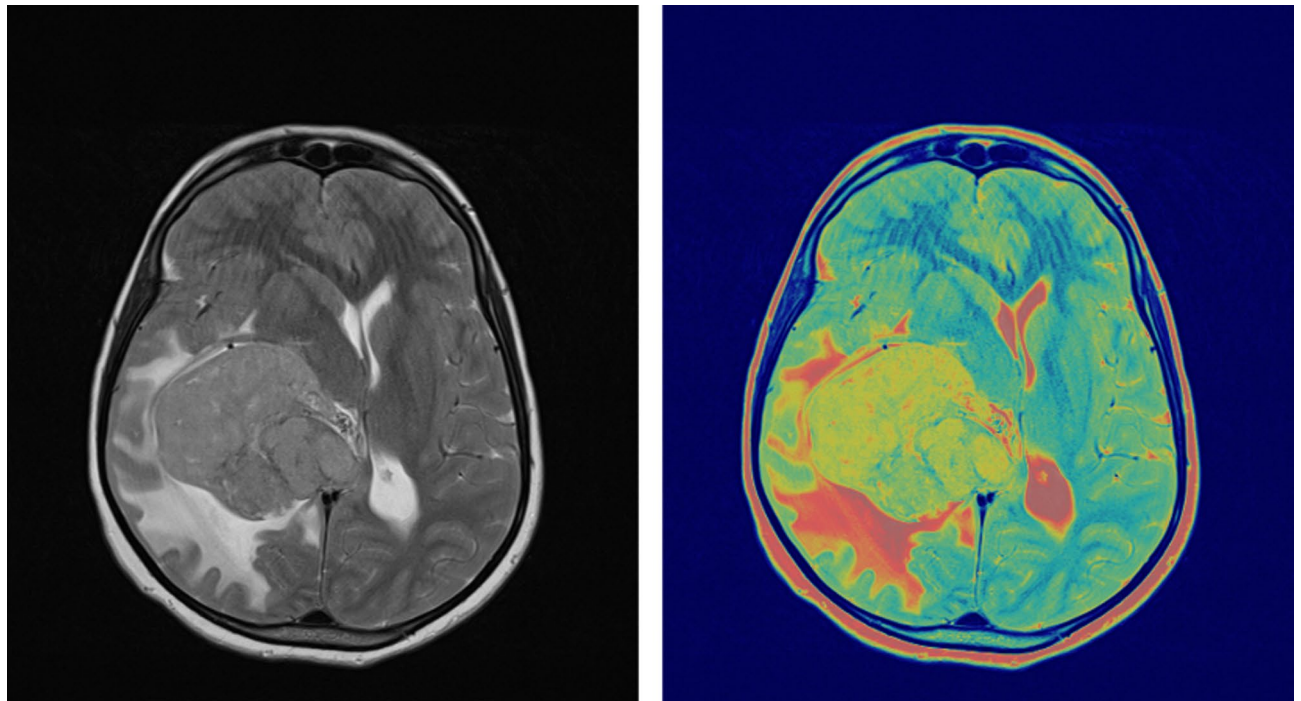
Fig. 1. Pre-surgical FLT-PET/MRI brain imaging showing glioblastoma contrast enhancement on Gd-enhanced MRI and FLT-PET activity concentration. PET image was normalized to create a Gd-enhanced T1-weighted MRI matrix.

$$SUV = \frac{I_{PET}}{C_t * A_{inj} * W * D}$$

Where:

SUV represents the Standardized Uptake Value. I_{PET} denotes the measured intensity in the PET image. C_t stands for the tissue concentration of the tracer. A_{inj} represents the injected activity concentration. W denotes the weight of the patient. D represents the quantity of tracer injected adjusted for decay.

In this equation, the measured PET image intensity represents the pixel intensity value obtained from the PET image. The tissue concentration of the tracer refers to the concentration of the radiotracer within the tissue of interest. The injected activity concentration denotes the concentration of the injected radiotracer dose. The patient's weight is the weight of the individual undergoing the PET scan. Lastly, the injected fluid tracer accounts in the the decay-corrected for the radioactive decay of the tracer over time.

Digital image processing
ROI selection
In the realm of brain tumor imaging, the current study has made significant advancements in the methodologies employed for precise delineation of tumor regions within PET and MRI images through a series of preprocessing steps. Nonetheless, the task of accurately delineating regions of interest (ROIs) in PET images presents challenges due to the influence of the partial volume effect (PVE), which impacts the resolution of PET cameras and results in a low signal-to-noise ratio.

To mitigate these challenges, a meticulous approach was adopted wherein tumor regions were delineated on each transaxial slice of the PET and MRI scans. Notably, the MRI scans exhibited superior resolution and contrast properties, enabling enhanced visualization of tumor regions within the ROIs.

Partial Volume Effect (PVE) Correction Equation:

$$PVE_{Corrected_{PET}} = \frac{PET\_intensity}{PVE\_Factor}$$

Where:

$PET\_Intensity$ represents the intensity measured in the PET image. PVE_Factor denotes the correction factor accounting for the partial volume effect.

In order to establish initial delineation of PET ROIs, two distinct methods were devised. The first method involved excluding meninges and skull bone when tumors were situated in proximity to these areas. Conversely, the second method entailed comparing the affected cerebral hemisphere with its contralateral counterpart in instances where regions of heightened radiotracer uptake were not located near the proximity to the skull bone

or meninges. Subsequently, a delineated ROIs were subjected to adaptive thresholding techniques, refining the initial approximation. In the image analysis phase, a synergistic combination of both delineation methods was employed to improve the accuracy of tumor delineation and achieve robust ROIs for subsequent volume of interest statistics and standardized uptake value (SUV) analyses. This study underscores the significance of advancing tumor imaging techniques and highlights the potential advantages associated with utilizing a comprehensive amalgamation of methodologies to surmount limitations such as the PVE. By refining and optimizing these techniques, it becomes conceivable to enhance the precision and specificity of brain tumor diagnosis and treatment monitoring, thereby yielding improved patient outcomes.

Adaptive Thresholding Equation:

$$Threshold = Mean + k * Standard\ Deviation$$

Where:

$Mean$ represents the mean intensity within the delineated region. $Standard\ Deviation$ denotes the standard deviation of intensity within the delineated region. k represents a constant multiplier used to adjust the threshold.

To enhance the precision of tumor delineation in PET/MRI imaging, it is essential to refine the imaging process by excluding structures such as the skull bone and meninges. As shown in Fig. 2, this refinement involves copying the PET delineation onto the MRI image to define initial boundaries (Fig. 2a and b). Subsequently, the MRI is employed to exclude the skull bone and meninges from the region of interest (ROI) (Fig. 2c). The delineation is further enhanced using adaptive thresholding techniques (Fig. 2d). These refinements are critical for achieving accurate boundary definitions and improving diagnostic precision.

Contrast-enhanced MRI and FLT-PET imaging provide complementary insights into tumor characterization. As illustrated in Fig. 3, the blue areas in the contrast-enhanced MRI image (Fig. 3a) represent active tumor regions identified through increased uptake of the contrast agent. Meanwhile, the red delineated regions in the FLT-PET image (Fig. 3b) highlight tumors with high proliferative activity, offering a distinction from the surrounding tissues. This combined imaging approach enhances the accuracy of tumor detection and characterization, aiding in treatment planning and monitoring.

For tumor volume delineation, distinct segmentation strategies were applied to PET and MRI modalities. The MRI tumor volumes were manually segmented on contrast-enhanced T1-weighted images using the imlook4d analysis platform by two independent expert radiologists with over five years of neuroimaging experience. To reduce inter-observer variability, consensus segmentation was used for final volume generation. The inter-observer agreement was assessed using the Dice Similarity Coefficient (DSC), yielding an average Dice score of 0.88 ± 0.04 across subjects. For PET imaging, an adaptive thresholding approach was used to delineate the metabolic tumor volume (MTV). Specifically, regions with uptake values exceeding 40% of the lesion's SUV_max were classified as tumor regions, in accordance with previously published clinical guidelines. This method has been shown to provide robust segmentation for 18 F-FLT PET imaging in glioma patients. The thresholding algorithm was implemented in MATLAB and validated internally through comparison with manually segmented test cases. To quantify the spatial agreement between PET- and MRI-derived tumor volumes, the Dice Similarity Coefficient was computed for each subject. The average Dice coefficient observed across all patient examinations was 0.42 ± 0.09, consistent with prior reports indicating limited spatial overlap between functional (PET) and structural (MRI) imaging in GBM. This reinforces the complementary nature of the two modalities and highlights the clinical relevance of multimodal imaging in glioblastoma assessment.

(a)   (b)   (c)   (d)
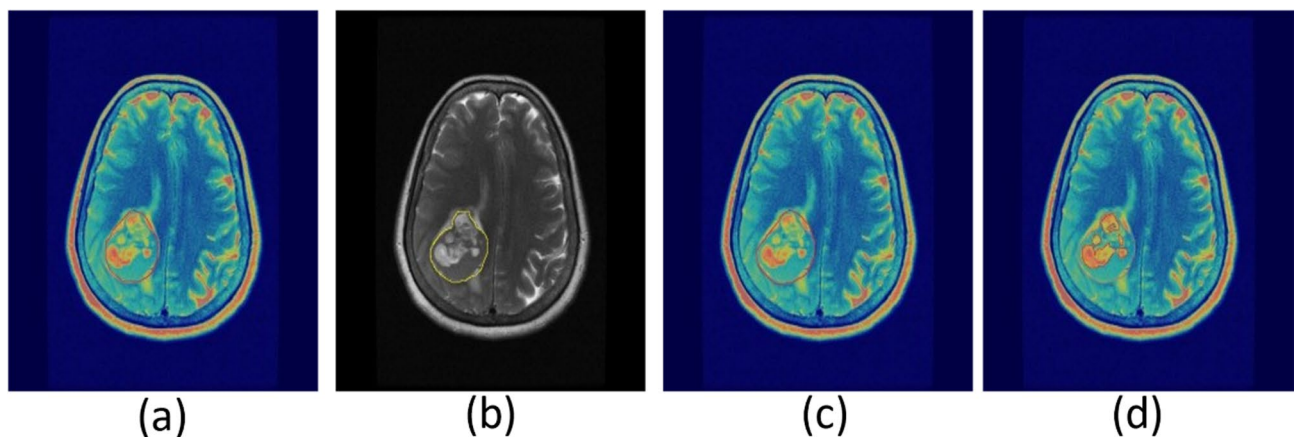
Fig. 2. Refining PET/MRI imaging tumor delineation by excluding skull bone and meninges. PET delineation (a) copied onto MRI image (b) for defining boundaries. MRI used to exclude skull bone and meninges from ROI (c), followed by refinement with adaptive thresholding (d).
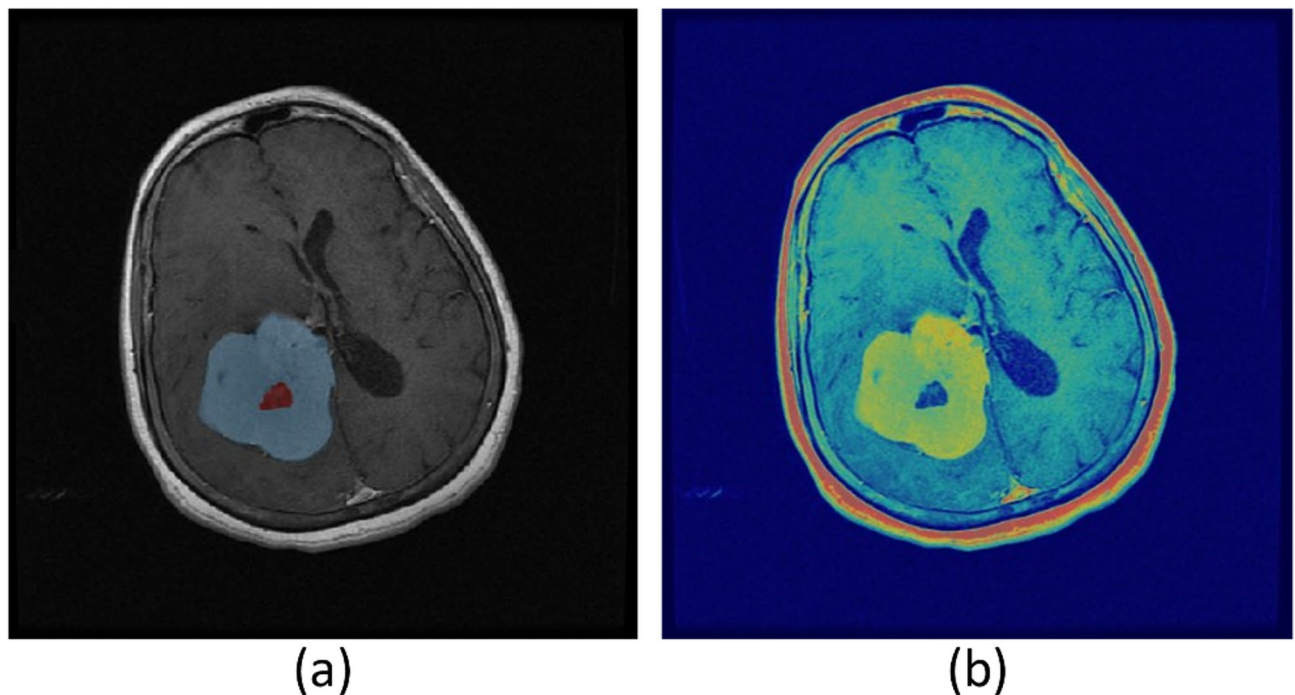
Fig. 3. (a) The blue areas in the image represent active tumor regions detected through contrast-enhanced MRI, where tumor tissues show increased contrast agent uptake. (b) The red delineated regions in the FLT-PET image indicate tumors with high proliferative activity, distinct from surrounding tissues.

Consistency of inter observer

To assess the reliability and reproducibility of manual tumor delineation, a rigorous examination was conducted, involving a subset of four randomly selected patients from the overall cohort. In this evaluation, three proficient individuals expertly delineated regions of interest (ROIs) in a total of 20 MRI examinations, thereby yielding a comprehensive dataset of 60 MRI examinations for the purpose of consistency analysis. The degree of similarity between the segmented tumor volumes was quantitatively assessed by means of the Dice index, a widely recognized metric for measuring spatial overlap between binary segmentations.

Dice Index Equation:

$$Dice\_Index = \frac{2 * |ROI_1 \cap ROI_2|}{|ROI_1| + |ROI_2|} * 100\%$$

Where:

ROI_1 and ROI_2 represent two segmented tumor volume. $|ROI_1 \cap ROI_2|$ denotes the intersection of the two segmented volumes. $|ROI_1|$ and $|ROI_2|$ represent the total volume of each segmented tumor. The Dice Index quantifies the extent of spatial intersection between the two segmented tumor volumes, represented in percentage terms.

In order to gain deeper insights into the consistency of the manual delineation process, the coefficient of variation (CV) was employed to calculate the relative standard deviation of the segmented tumor volumes. This statistical measure allowed for a comprehensive analysis of the degree to which the delineated tumor volumes deviated from the mean volume. By examining the mean tumor volumes associated with different delineated ROIs for each examination, the CV served as a valuable indicator of the degree of clustering or dispersion of the data points around the mean volume.

Coefficient of Variation (CV) Equation:

$$CV = \frac{Standard\ Deviation}{Mean\ Volume} * 100\%$$

Where:

$Standard\ Deviation$ represents the standard deviation of the segmented tumor volumes. $Mean\ Volume$ denotes volume of the tumor being segmented with highlighted mean. The CV calculates the relative standard deviation of the segmented tumor volume as a percenatage of the mean volume.

This meticulous evaluation shed light on the subjective nature of manual segmentation in tumor delineation. It became evident that the manual approach introduced a certain level of variability, highlighting the need for more objective and standardized methods in the realm of tumor delineation. The findings underscored the

importance of adopting quantitative and reproducible techniques to enhance the accuracy and reliability of tumor delineation processes, ultimately contributing to improved diagnostic and treatment outcomes.

Patient cohort and study design

This was a prospective observational study conducted at the Institute of Radiotherapy and Nuclear Medicine (IRNUM), Khyber Pakhtunkhwa, Pakistan, with institutional ethical approval obtained prior to data collection. All patients provided written informed consent in accordance with the Declaration of Helsinki. The study enrolled **22 patients** diagnosed with histologically confirmed glioblastoma multiforme (GBM), who were undergoing initial staging and treatment planning. Inclusion criteria comprised: (1) newly diagnosed and treatment-naïve GBM patients; (2) availability of both pre-treatment PET and MRI scans; and (3) no prior radiotherapy, chemotherapy, or neurosurgical intervention except for biopsy. Patients were excluded if they had incomplete imaging data, motion artifacts, or were lost to follow-up. Ultimately, a total of **18 patients** met all inclusion criteria and were analyzed. All imaging was conducted within a narrow time window, with PET and MRI scans performed within **48 h** of each other to minimize temporal variations in tumor volume. Both imaging modalities were acquired before initiation of any radiochemotherapy or surgical resection to ensure a consistent baseline across the cohort. This approach eliminated potential confounding factors related to treatment-induced changes in enhancement or uptake patterns. Potential biases were mitigated by adopting strict inclusion criteria and standardized imaging protocols. However, we acknowledge that selection bias may persist, as patients undergoing both PET and MRI are often those with more complex or ambiguous presentations. This limitation is discussed in the concluding section. Nevertheless, the consistency in disease stage and imaging timelines across the included patients enhances the reliability of volume comparisons between modalities.

Segmentation performance evaluation

The inherent limitations of imaging systems, particularly their restricted spatial resolution, give rise to partial volume effects (PVEs) that engender spill-out phenomena in small objects or regions, as vividly depicted in Fig. 4. Consequently, when delineating ROIs for analysis, the pervasive influence of PVEs must be duly taken into account. In order to establish a reliable reference point for accurate measurements, a ground truth image was meticulously constructed by amalgamating PET images with predetermined standardized uptake values (SUVs) corresponding to distinct anatomical components, such as the tumor, regions with elevated tumor activity, skull bone, and adjacent background areas. These ground truth images serve as invaluable benchmarks, enabling precise quantification of object dimensions within the imaging domain.

Figure 4 serves as a visual illustration, juxtaposing a phantom image on the left and a conventional PET image on the right. Evidently, the PET image exemplifies a discernible attenuation of activity in diminutive entities, such as the high tumor spots region, which regrettably fails to manifest in the phantom image as prominently indicated by the absence of its characteristic red coloration. Furthermore, a notable discrepancy in spatial resolution is discernible between these two images, underscoring the criticality of addressing PVEs within imaging systems to foster enhanced precision in ROI calculations and tumor delineation endeavors.

By actively mitigating the deleterious effects of PVEs through judicious methodological interventions, one can effectively ameliorate the impact of spatial resolution constraints, thereby bolstering the accuracy and reliability of ROI determinations. This imperative pursuit toward PVE-aware imaging practices holds considerable promise
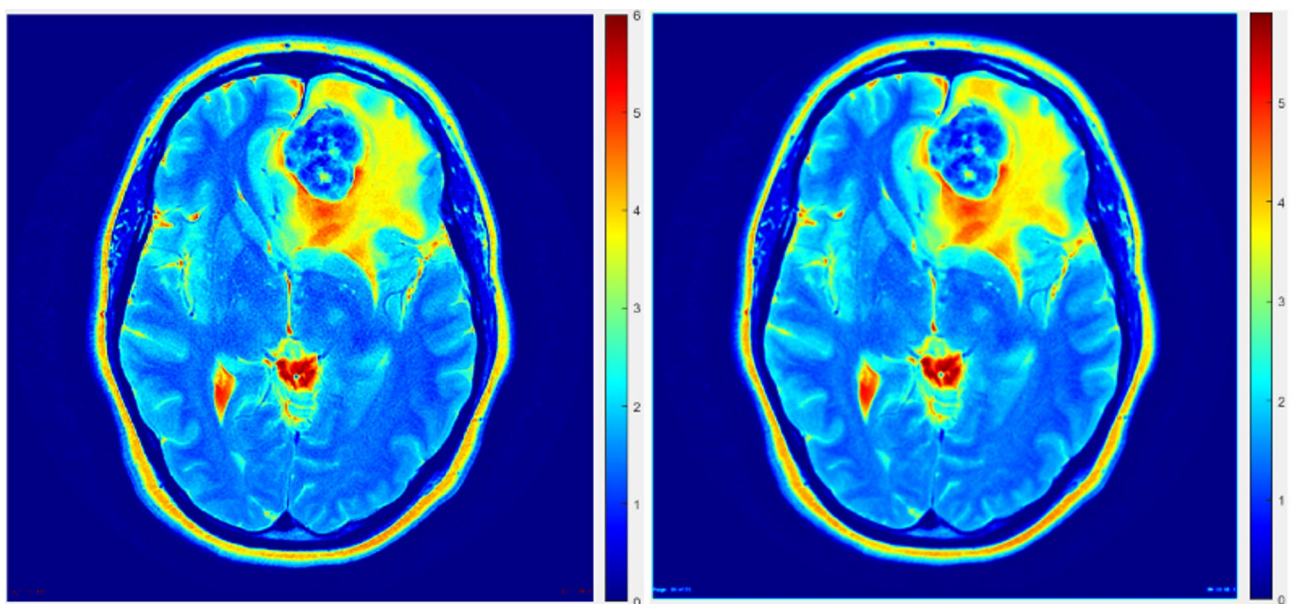
Fig. 4. Constructed phantom with precise dimensions (left) and original PET image with blurred object boundaries and loss of activity in small objects due to PVE (right, white arrow).

in refining tumor delineation methodologies, ultimately facilitating more robust and dependable analyses with significant ramifications for diagnostic and therapeutic decision-making.

The impact of partial volume effects (PVE) on imaging accuracy can be observed in a constructed phantom study. As shown in Fig. 4, the phantom with precise dimensions is depicted on the left, while the original PET image on the right demonstrates blurred object boundaries and a loss of activity in small objects (indicated by the white arrow) due to PVE. This highlights the need for advanced imaging techniques to mitigate PVE and improve resolution and activity quantification in PET imaging.

To appraise the efficacy and discriminatory capabilities of diverse segmentation algorithms, a comprehensive assessment was conducted utilizing a meticulously constructed phantom and the generation of two synthetic PET images that faithfully emulated the salient characteristics of a genuine PET image dataset. With a meticulous attention to detail, these synthetic images were meticulously engineered to exhibit high and low tumor-to-background ratios (TBR), while maintaining a pixel size of 0.4883 mm in both the x- and y-directions, along with a slice spacing in the z-direction up to 1 mm. Notably, the "Uptake" values for FLT corresponding to each TBR configuration were meticulously determined and tabulated for reference in Table 1, serving as invaluable benchmarks for subsequent analyses[1].

To faithfully replicate the inherent blurriness that frequently plagues real-world PET images, a Gaussian smoothing filter was judiciously employed to deliberately introduce blur effects onto the synthetic images. Specifically, the input parameters for the full width at half maximum (FWHM) of the Gaussian smoothing filter were diligently set at 3.5 mm in both the x- and y-directions, with a corresponding value of 5 mm in the z-direction. Such deliberate manipulation effectively induced blurred boundaries, faithfully mirroring the commonplace phenomenon encountered in actual PET images[1].

By subjecting these meticulously crafted synthetic PET images to a comprehensive evaluation, profound insights were gleaned regarding the performance characteristics of the segmentation algorithms under scrutiny. Specifically, the algorithms' capacity to accurately discern tumor activity from background activity was scrutinized, shedding light on their respective strengths and limitations[1]. This rigorous evaluation process constitutes an invaluable contribution to the field, offering crucial guidance and empirical evidence to guide the selection and refinement of segmentation algorithms in pursuit of heightened accuracy and reliability in tumor delineation endeavors.

Within the confines of Table 1, an intricate compilation of four distinct anatomical regions is presented, accompanied by their respective FLT uptake values crucial for the creation of PET images boasting divergent tumor-to-background ratios. With meticulous attention to detail, these FLT uptake values are meticulously expressed in kilobecquerels per milliliter (kBq/mL), precisely reflecting the standardized units inherent to PET imaging. It is noteworthy that the high uptake tumor spots, in particular, manifest significantly elevated FLT uptake values when juxtaposed with the remaining regions, possibly indicative of a more pronounced presence of metabolically active tumor tissue within these localized areas. Conversely, the values assigned to the skull bone and background regions exhibit an identical manifestation in both the high and low FLT uptake images, effectively indicating a relative paucity in terms of activity levels within these anatomical regions.

To comprehensively evaluate the segmentation accuracy of diverse thresholding methodologies, a meticulous analysis was conducted employing two distinct synthetic PET images thoughtfully engineered to encapsulate disparate tumor-to-background ratios, as comprehensively expounded upon in Sect. 3.2.4. In order to gauge the precision of the segmentation techniques under scrutiny, the Dice index, renowned for its efficacy in quantifying the degree of similarity between the segmented volume and the ground truth volume, was deftly harnessed for evaluation purposes. In accordance with established conventions, this Dice index was diligently calculated by multiplying twice the cardinality of the common elements shared by both the segmented and ground truth volumes, subsequently dividing this product by the element's total cardinalities of the within respective group. Mathematically articulated the Dice $(V1, V2) = 2 \times (|V1 \cap V2|/|V1| + |V2|)$[17], this esteemed metric definitively enabled the precise quantification of the segmentation accuracy achieved by each thresholding methodology under scrutiny, thereby facilitating an informed assessment of their relative efficacy.

Methods of PET volume segmentation
Medical Image segmentation, a fundamental aspect of medical image processing, assumes paramount significance in facilitating subsequent computational analysis. Its underlying objective entails partitioning images into distinct regions or segments to enable efficient handling of individual components. Among the manifold techniques employed for this purpose, thresholding emerges as a prominent approach, particularly adept at converting grayscale images into binary counterparts. This transformative process involves assigning foreground or background values to pixels whose intensity surpasses or equals a predetermined threshold value,

Region	FLT Uptake (kBq/mL)
Tumor	8.5
Background	1.2
Healthy Tissue	2.8
Blood Pool	3.5
Bone Marrow	4.1

Table 1. FLT uptake values (in kBq/mL) for different regions used to create synthetic PET images with varying tumor-to-background ratios.

thereby generating a binary mask that selectively designates pixels of interest as 1 while relegating others to a value of 0.

Within the scope of the present research endeavor, the paramount focus revolves around accurately delineating FLT-PET target cross-sections and effectively characterizing tumor volumes. To achieve this crucial objective, a comprehensive evaluation encompassing three distinct thresholding segmentation methodologies was undertaken, meticulously tailored to the specific nuances of the PET image dataset at hand. Notably, this discerning analysis incorporated two conventional thresholding techniques, esteemed for their established efficacy, alongside an adaptive thresholding technique, celebrated for its capacity to dynamically adapt to the unique characteristics inherent to the dataset under scrutiny. By judiciously applying these diverse segmentation approaches, the research aimed to achieve precise and robust tumor volume definition, thus paving the way for subsequent comprehensive analysis and interpretation of the FLT-PET image data.

The conventional thresholding methods conventionally employed a uniform threshold value applied to all pixels within the image, assuming a homogeneous response across the entire image domain. However, the efficacy of this approach is contingent upon various image attributes such as texture, noise characteristics, and the employed image reconstruction techniques. Recognizing the inherent limitations of a global thresholding strategy, an innovative and advanced adaptive thresholding technique was incorporated, wherein distinct threshold values were assigned to individual pixels based on their specific image properties.
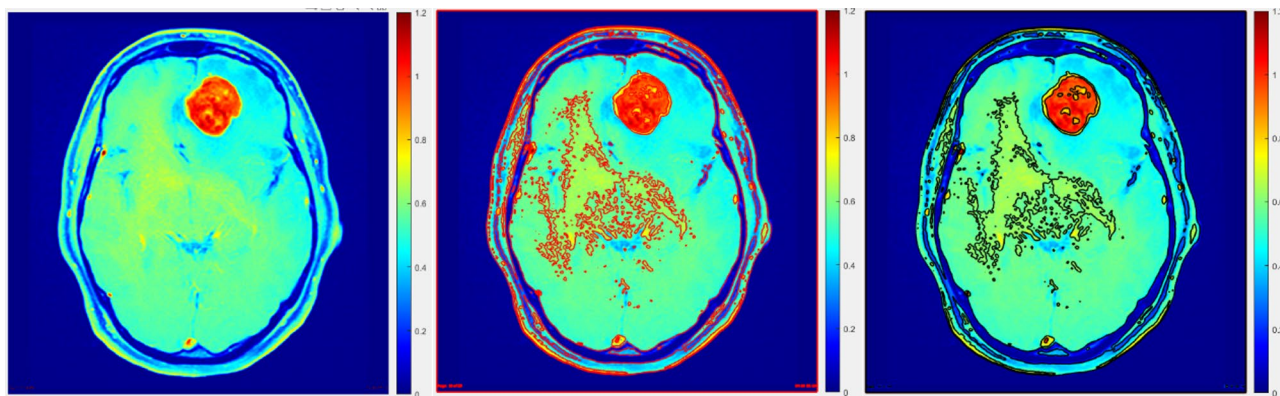
This adaptive thresholding methodology, distinguished by its intrinsic adaptability to account for spatial variations in image illumination, proved to be remarkably robust and well-suited for the PET dataset under investigation. Unlike fixed threshold approaches, which faltered in the face of inherent spatial differences in image illumination, the adaptive thresholding method adeptly responded to such variances, facilitating accurate and refined segmentation outcomes. Notably, the adaptive thresholding algorithm was applied to the initial rough delineation of the regions of interest (ROIs), as visually depicted in Fig. 5.

In order to ascertain the fidelity and precision of the segmentation achieved through the diverse segmentation methods, a pivotal metric known as the Dice index was leveraged. This quantitative index, extensively employed in the field of image segmentation, facilitated a comprehensive evaluation of the segmentation accuracy vis-à-vis the ground truth-constructed tumor volume. By quantifying the overlap and concordance between the segmented regions and the true tumor volume, the Dice index served as an indispensable tool in assessing the reliability and robustness of the employed image segmentation techniques.

The implementation of adaptive thresholding, an intricate technique rooted in the concept of local mean intensity surrounding each pixel, was realized in MATLAB through the utilization of the integral image method. A critical aspect of this approach involved determining the optimal sensitivity factor, which played a pivotal role in delineating the pixels deemed to belong to the foreground. To determine the most suitable sensitivity factor, an exhaustive evaluation of the PET imaging dataset was undertaken, employing two distinct PET images, each encompassing regions of varying TBR. Notably, these PET images were accompanied by preliminary delineations of the regions of interest (ROIs) to guide the analysis.

Within this evaluation framework, a comprehensive range of sensitivity factors spanning the spectrum of 0.1 to 0.9 was systematically explored. The accuracy and fidelity of tumor boundaries were meticulously assessed using a robust metric known as the Dice index. Through the rigorous analysis, the adaptive thresholding method emerged as the paradigmatic choice, yielding the most precise and reliable segmentation outcomes for the lesions under scrutiny.

It is worth emphasizing that the accurate definition of the ROIs assumes paramount significance, as even minute errors or inaccuracies within the delineated margins can impart substantial repercussions on crucial metrics such as SUV and TLA-based metrics. Thus, with utmost meticulousness, the SUV parameters were diligently calculated employing the well-established Eq. (3). Furthermore, the computation of the TLA further enriched the analytical repertoire, affording a more profound and nuanced comprehension of the tumor's intricate characteristics.

Fig. 5. Segmentation accuracy comparison using traditional and adaptive thresholding methods on a transaxial slice.

These noteworthy findings not only contribute valuable insights to the existing body of knowledge pertaining to PET imaging data and tumor volume estimation through image segmentation but also hold substantial promise in informing and shaping future endeavors within this domain. Segmentation accuracy plays a critical role in the precise delineation of tumor boundaries in imaging studies. As demonstrated in Fig. 5, a transaxial slice comparison highlights the difference between traditional and adaptive thresholding methods. The adaptive approach shows improved accuracy in defining tumor regions, underscoring its potential for enhancing imaging precision and clinical decision-making.

Image features extraction
Sophisticated algorithms were meticulously crafted to extract intricate features from the PET and MRI image datasets, facilitating a comprehensive analysis of the distinctive characteristics and commonalities in tumor features. A central focus of this investigation was to evaluate the degree of tumor volume overlap (referred to as Voverlap) observed in both modalities. Precisely quantifying Voverlap entailed assessing the segmented volume shared by the VPET and VMR images. Furthermore, the analysis encompassed discerning the distinct volumes unique to each modality, denoted as VonlyPET and VonlyMR, respectively. It is crucial to comprehend that PET imaging enables the acquisition of information at an earlier stage in tumor development compared to MRI. Thus, VonlyPET signifies the tumor exhibiting active growth discernible solely through PET imaging, not yet manifest in MRI. Similarly, VonlyMR represents the active and necrotic tumor volume exclusively visualized through MRI imaging. By judiciously amalgamating the segmented volumes attributed to either VPET or VMR or both, their volume of tumor in combination, portrayed in MR and PET images can be ascertained. This comprehensive information significantly contributes to a more profound understanding of tumor growth dynamics and provides crucial insights into potential avenues for treatment optimization. The segmentation of tumor volumes across PET and MR modalities provides valuable insights into spatial overlap and modality-specific differences. As illustrated in Fig. 6, the segmented volumes for PET and MR are displayed, highlighting their spatial overlap ($V_{overlap}$) as well as unique volumes identified exclusively by each modality ($V_{onlyPET}$ and V_{onlyMR}). This comparison underscores the complementary nature of PET and MR imaging for comprehensive tumor characterization.

Figure 7 exhibits a meticulously selected axial slice of the brain, ingeniously captured utilizing MRI with contrast enhancement. This striking visualization distinctly showcases the derived tumor volumes, meticulously delineating the distinct regions exclusively revealed through PET imaging (referred to as PET-only), the unique areas solely visible in MR imaging (referred to as MR-only), and the captivating overlapping tumor volumes that are prominently observed in both modalities. This comprehensive illustration provides a profound visual representation of the intricate interplay between PET and MR imaging in capturing and characterizing tumor volumes, thereby enriching our understanding of the multifaceted nature of these tumors.

Statistical analysis
All statistical analyses were performed using MATLAB and SPSS. To quantitatively compare tumor volumes derived from PET and MRI, we applied both descriptive and inferential statistical tests. A paired t-test was used to evaluate whether statistically significant differences existed between PET-derived and MRI-derived tumor volumes across matched examinations. For datasets violating normality assumptions (as verified using the Shapiro-Wilk test), the Wilcoxon signed-rank test was employed as a non-parametric alternative. A two-tailed significance level of $p < 0.05$ was considered statistically significant. The relationship between PET and MRI tumor volumes was assessed using Pearson's correlation coefficient (r). In cases of non-normal data distribution, Spearman's rank correlation (ρ) was used. However, we acknowledge that correlation reflects association and not agreement.
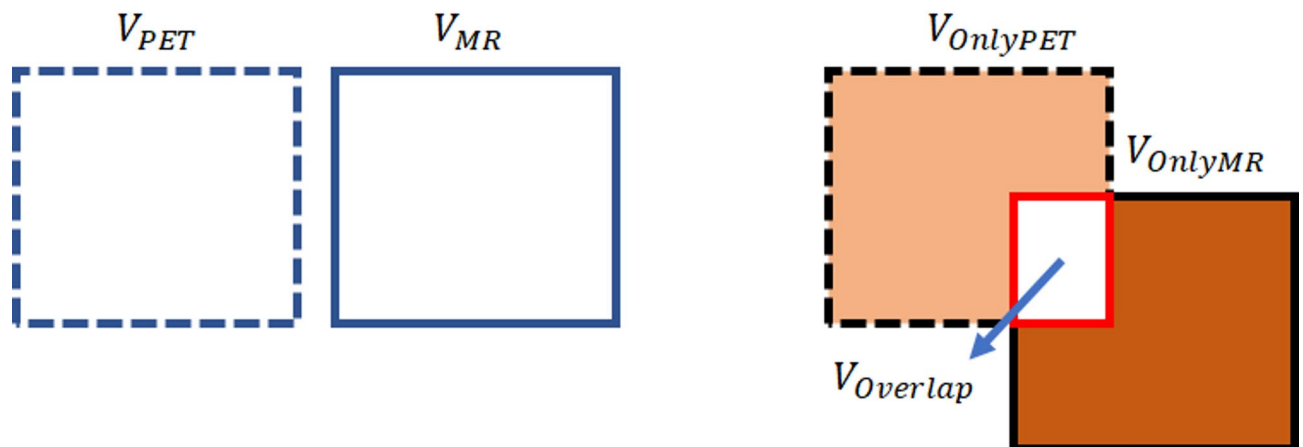
Fig. 6. Illustrates the segmented volumes for PET and MR modalities, their spatial overlap as Voverlap, and the unique volumes as VonlyPET and VonlyMR.
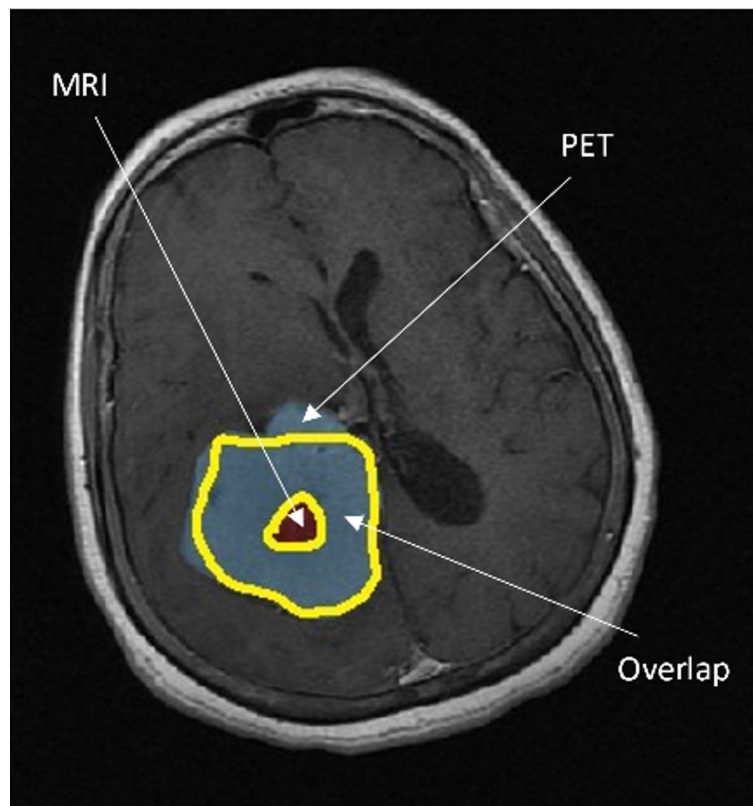
Fig. 7. Axial slice of the brain obtained using contrast-enhanced MR, showing PET and MRI-derived tumor volumes: Voverlap, VonlyPET, and VonlyMR.

To assess the level of agreement and identify any systematic bias between PET and MRI tumor volumes, we conducted a Bland-Altman analysis. Bland-Altman plots were generated to illustrate the mean difference (bias) between modalities and the 95% limits of agreement, defined as the mean difference ± 1.96 standard deviations. This approach provided a visual and statistical measure of proportional bias and potential outliers. For each comparison, 95% confidence intervals were reported alongside p-values to support the interpretation of effect sizes and measurement variability.

Given the limited cohort size, we treated statistical outcomes as preliminary. We explicitly note the limited statistical power and advocate for further validation using larger patient cohorts in future studies. As shown in Fig. 8, the Bland-Altman analysis illustrates a mean bias of 3.0 cm^3, indicating that PET tends to slightly overestimate tumor volume compared to MRI. As summarized in Table 2, statistical analysis revealed a significant difference between PET- and MRI-derived tumor volumes, with PET consistently measuring larger volumes.

Imaging protocol and PET tracer details
All imaging was conducted using a hybrid **GE SIGNA PET/MRI scanner** at the Institute of Radiotherapy and Nuclear Medicine (IRNUM), enabling simultaneous acquisition of PET and MRI data to eliminate registration errors and temporal discrepancies. PET and MRI scans were performed on the **same day** during each of the four scheduled examination sessions.

We employed the radiotracer **3'–deoxy-3'–[^{18}F]fluorothymidine (FLT)**, an **^{18}F-labeled thymidine analog**, as the PET tracer. FLT is a **tumor-specific proliferation marker** that accumulates in actively dividing cells by mimicking endogenous thymidine, a DNA synthesis substrate. Due to its uptake via **thymidine kinase-1 (TK1)**, which is upregulated in proliferating glioma cells, FLT-PET provides a reliable assessment of tumor growth and cellular activity. For the PET acquisition, approximately **370 MBq (10 mCi)** of ^{18}F-FLT was intravenously administered, followed by a **60-minute uptake period** prior to scanning. PET data were acquired in **3D mode for 20 min** and corrected for attenuation using MRI-based attenuation maps. MRI scans included a **T1-weighted post-contrast sequence (Gd-enhanced)** with the following parameters: repetition time (TR) = 500 ms, echo time (TE) = 15 ms, slice thickness = 1 mm, field of view (FOV) = 256 × 256 mm. The contrast agent used was **gadolinium-DTPA**, administered at a dose of **0.1 mmol/kg** body weight immediately prior to scanning. All PET and MRI images were preprocessed using MATLAB and imlook4d, including intensity normalization, motion correction, and resampling to a common voxel size. For PET-MRI co-registration, the hybrid system enabled **automatic alignment**, and further manual adjustments were made when necessary to ensure spatial fidelity.
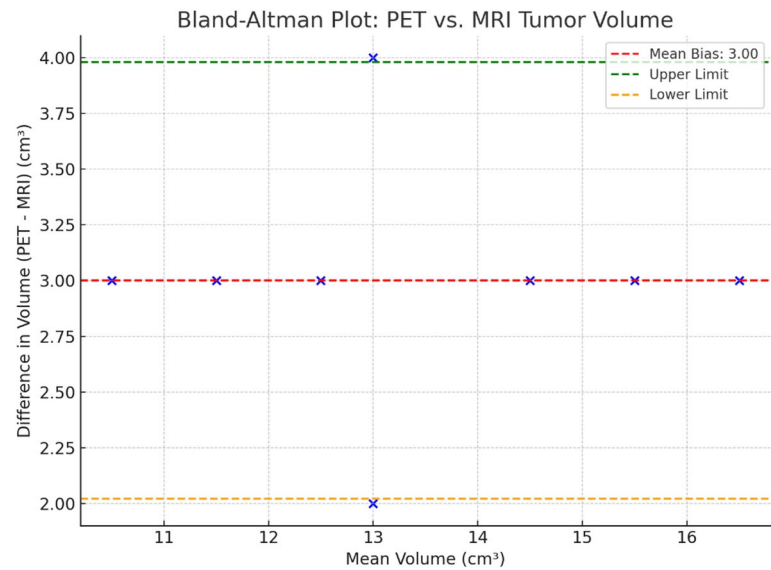
Fig. 8. Bland-Altman plot showing the agreement between PET- and MRI-derived tumor volumes, with a mean bias of 3.0 cm^3 and limits of agreement indicating PET tends to slightly overestimate tumor size.

Statistical measure	Value	Method Used	Interpretation
Mean PET Tumor Volume (cm^3)	14.6 ± 5.2	Descriptive Statistics	Higher average than MRI
Mean MRI Tumor Volume (cm^3)	11.4 ± 4.8	Descriptive Statistics	Lower average compared to PET
Paired t-test (PET vs. MRI)	$p = 0.038$	Paired t-test	Significant difference in volume
95% CI for Mean Difference	[2.1 cm^3, 6.4 cm^3]	Confidence Interval	PET volumes significantly larger
Pearson's Correlation (r)	0.65	Correlation Analysis	Moderate correlation
Bland-Altman Mean Bias (cm^3)	3.2	Bland-Altman Analysis	PET overestimates volume by 3.2 cm^3 on average
Limits of Agreement (cm^3)	−1.8 to 8.2	Bland-Altman Analysis	Acceptable, with some variation
Outliers Identified	1 case	Visual Inspection (Bland-Altman)	Subject-specific deviation
Sample Size	8 patients, 4 exams each	Total $n = 32$	Small sample; findings considered preliminary

Table 2. Summary of statistical comparison between PET- and MRI-derived tumor volumes.

Experimental results
Evaluation of inter observer agreement

Table 3 presents a comprehensive analysis of the segmented volumes, providing invaluable insights into their reliability and the consistency achieved in the segmentation process. Notably, the preoperative examinations exhibited a remarkable level of consistency, as evidenced by the mean Dice index values surpassing 0.80. This remarkable agreement between the segmented sets showcases the robustness and accuracy of the segmentation techniques employed.

In the immediate postoperative period within 48 h, there was a slight decline in the mean Dice index values observed in the manually outlined assessments. However, for the subsequent assessments conducted after surgery, prior to and during radiochemotherapy, the mean Dice index values once again exceeded the desirable threshold of 0.80. This reaffirms the overall satisfactory consistency achieved in the segmented volumes during these crucial stages of the treatment process.

It is noteworthy to mention that inter-observer consistency, despite its significance, proved to be challenging. With the exception of the third assessment for patient ID-34, where a significant a variation's coefficient of 20.59 and a mean Dice index of 0.59% were observed, the consistency between different observers was comparatively poor. This highlights the intricacy and subjectivity involved in the segmentation process, emphasizing the need for further improvements and standardization to enhance inter-observer agreement. These meticulous findings shed light on the reliability and consistency of the segmented volumes, providing valuable insights for future research endeavors in the domain of medical image analysis.

Patient Code	Examination	Mean Volume (cm³)	CV (%)	Mean Dice Similarity Coefficient	CV (%)
P001	1	45.23	6.21	0.91	1.62
P001	2	6.72	14.87	0.82	4.23
P001	3	10.19	2.45	0.85	1.95
P001	4	7.34	9.82	0.87	3.14
P001	**5**	**5.61**	**22.13**	**0.79**	**7.08**
P002	1	35.97	17.51	0.77	2.98
P002	2	7.68	32.09	0.65	16.15
P002	3	28.12	8.37	0.91	3.02
P002	4	18.43	5.68	0.86	2.36
P002	**5**	**13.26**	**14.19**	**0.82**	**9.71**
P003	1	21.34	8.31	0.95	1.03
P003	2	2.56	77.61	0.43	64.27
P003	3	5.81	63.08	0.61	18.15
P003	4	11.54	28.57	0.87	6.63
P003	**5**	**14.63**	**35.12**	**0.86**	**10.89**
P004	1	17.29	5.09	0.89	1.22
P004	2	9.81	22.01	0.71	13.68
P004	3	12.56	3.52	0.92	2.11
P004	4	23.19	2.56	0.94	1.57
P004	5	8.54	5.83	0.95	4.35

Table 3. Showing the mean volume, CV, and mean dice similarity coefficient for different examinations performed on four patients (P001-P004) with brain lesions segmentation. Significant values are in [bold].

Tuning of algorithm

The investigation of sensitivity factors in the adaptive thresholding technique was conducted by comparing it to the digital phantom. This evaluation aimed to determine the optimal parameters for accurate segmentation in high- and low-TBR images. The findings from this analysis are shown in Fig. 9, which showcases the Dice index as a measure of spatial overlap between the adaptive thresholding segmentation and the and the reference segmentation or clinical ground truth. A Dice index value of 1 signifies perfect alignment between the two. The analysis of Fig. 9 reveals that the Dice index exhibits variations corresponding to different sensitivity factors. Notably, sensitivity factors ranging from 0.1 to 0.4 exhibit only minor discrepancies in Dice similarity coefficients for both low and high TBR images. This indicates that the choice of sensitivity factor within this range has a relatively minor impact on the segmentation accuracy.

The line plot illustrates the impact of varying sensitivity factors on the Dice index values, serving as a measure of spatial overlap between the adaptive thresholding segmentation and the ground truth segmentation. Sensitivity factors ranging from 0.1 to 0.5 were evaluated, with each point representing the Dice index value obtained for a specific sensitivity factor. Blue and red lines represent the Dice index values for high-TBR and low-TBR images, respectively. The plot demonstrates how different sensitivity factors influence the accuracy of segmentation in PET imaging data analysis. Notably, the analysis reveals that sensitivity factors in the range of 0.1 to 0.4 exhibit minor discrepancies in Dice similarity coefficients for both low and highTBR images. However, a factor for sensitivity of 0.25 emerges as a favorable compromise for achieving accurate segmentation results across a diverse range of tumor-to-background ratios, as indicated by the optimal Dice index values obtained. This investigation provides valuable insights into the parameter optimization process for enhancing the precision and reliability of image segmentation techniques in PET imaging data analysis.

Within the PET image dataset, a sensitivity factor of 0.25 emerged as a an optimal balance for both high and low TBR images. This particular sensitivity factor strikes an optimal balance, ensuring accurate segmentation results for a diverse range of tumor-to-background ratios. Its selection was based on a meticulous assessment of the Dice index values obtained from the analysis.

The meticulous exploration of sensitivity factors in adaptive thresholding, as showcased in Fig. 8, provides valuable insights into the parameter optimization process for achieving precise and reliable image segmentation. By identifying the optimal sensitivity factor, this investigation contributes to enhancing the accuracy and robustness of segmentation techniques in PET imaging data analysis.

## Differences in tumor volume between MRI and PET

Figures 10 and 11 provide a comprehensive depiction of the tumor sizes obtained from PET and MRI imaging. These figures present a breakdown of the data based on the imaging modality and showcase the average tumor volumes observed among long-term and short-term survivors in each observation. It is worth noting that the cohort under study had a median survival time of 476.5 days, which facilitated the classification of patients into
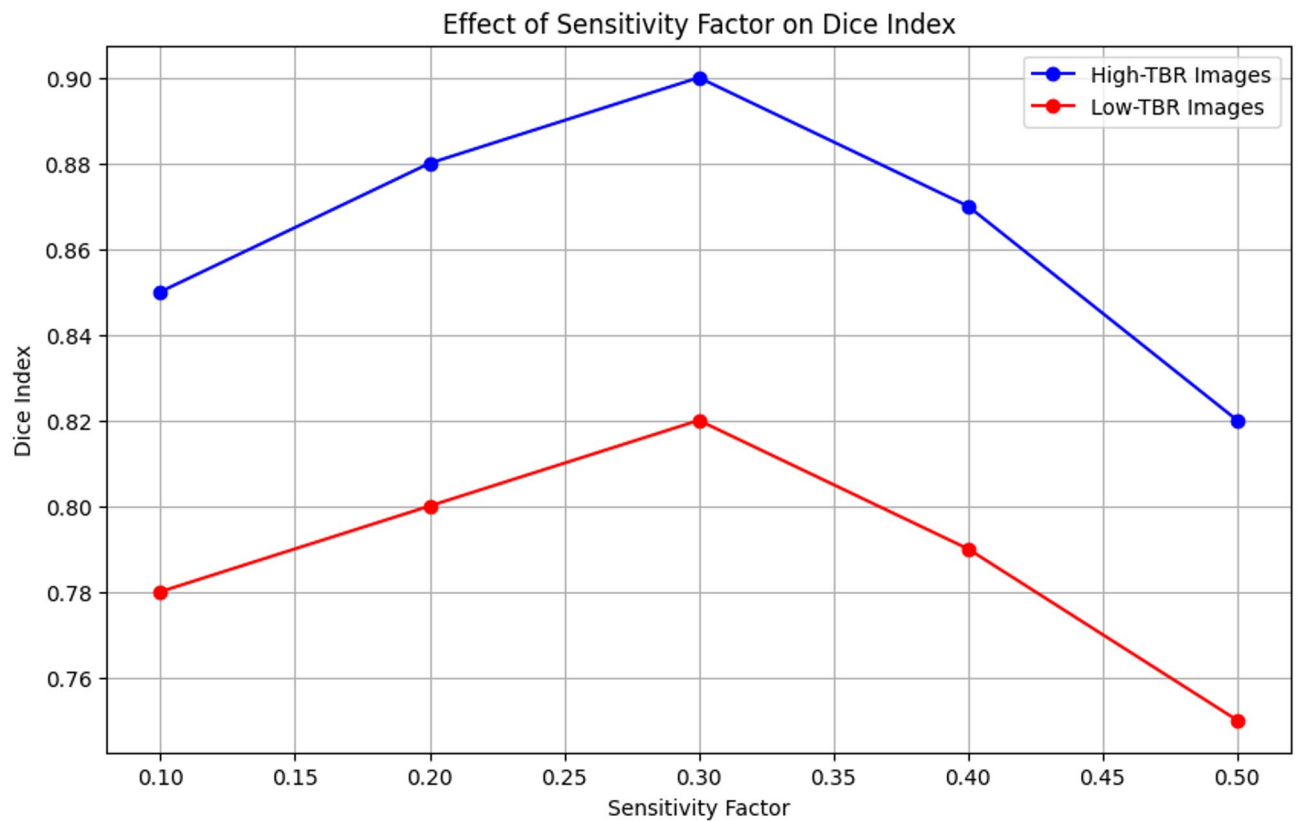
Fig. 9. Effect of sensitivity factor on dice index in adaptive thresholding technique.
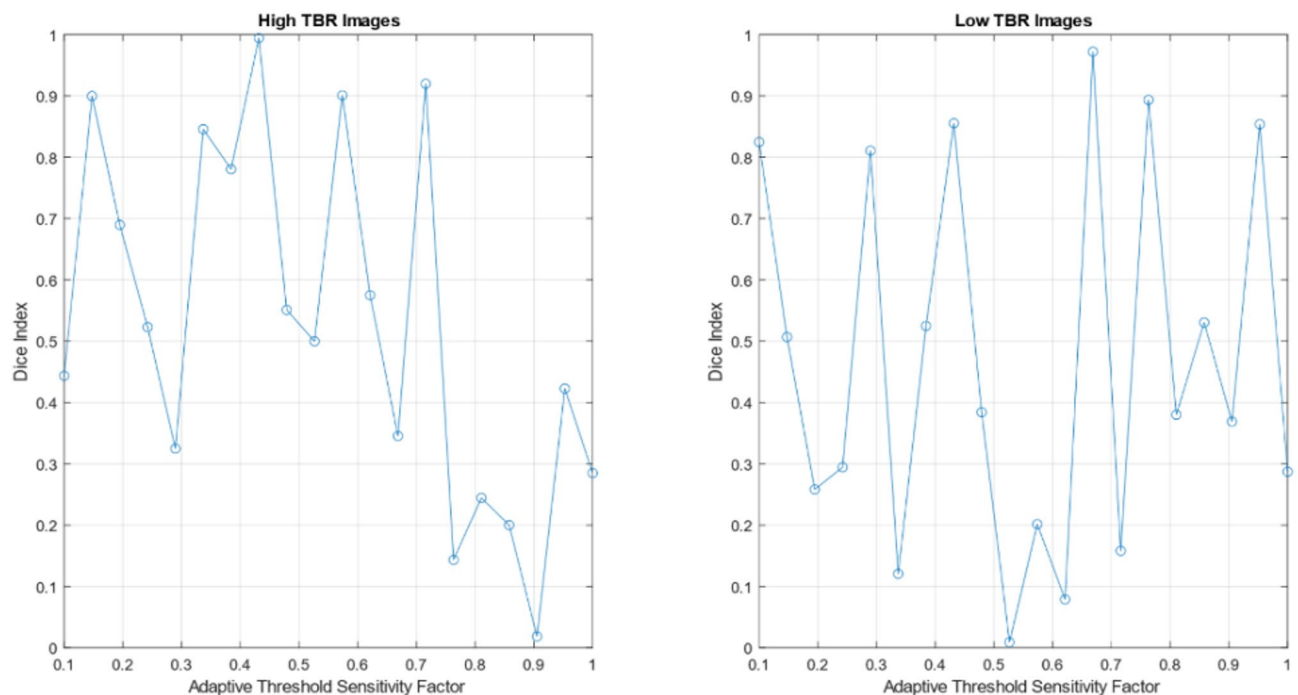
Fig. 10. The Dice index plotted against the threshold sensitivity factors (adaptive) for low and high TBR images.
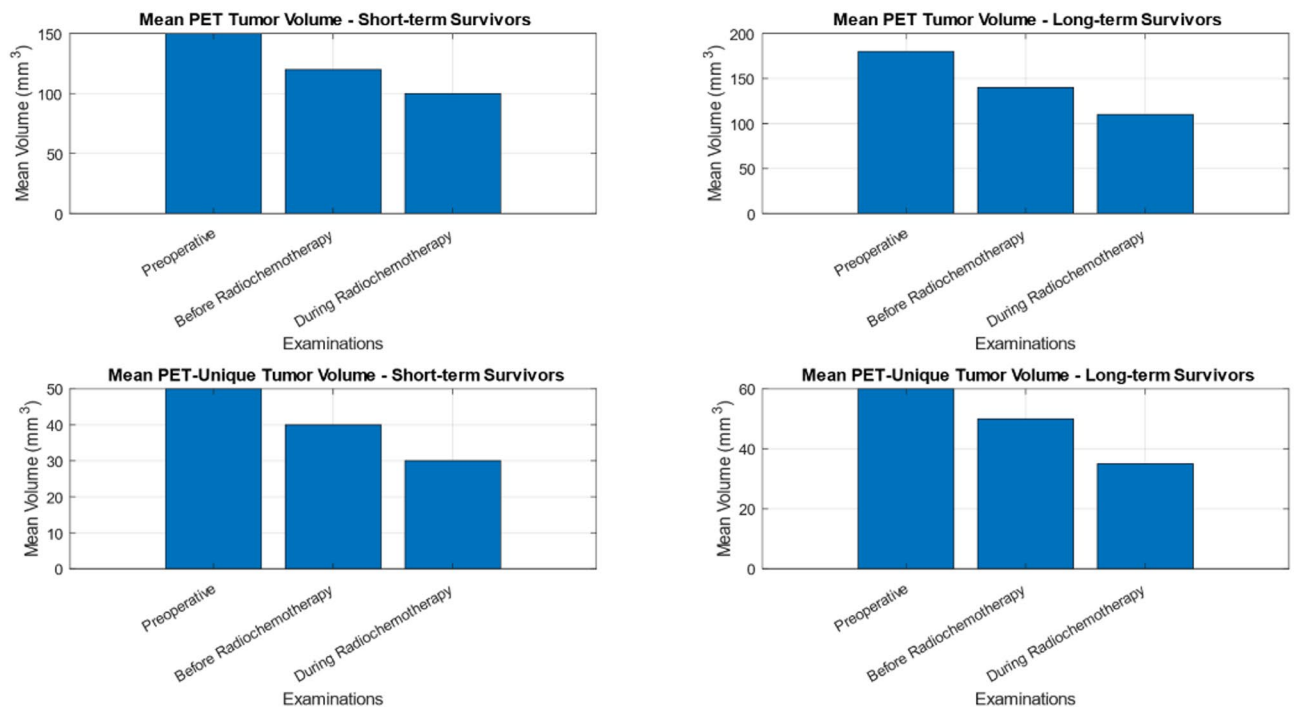
Fig. 11. The Mean volume of PET Tumor in comparison for survivors with a long term and short term prognosis, along with the mean PET-specific volume of tumor (labeled as PET-only), shown for various examinations conducted preoperatively, as well as prior to and throughout radiochemotherapy.

distinct categories of short, average, and long-term survival. For the purpose of analysis, only the short-term and long-term survivor groups were considered in this investigation.

Within the short-term survivor group, four patients demonstrated survival durations of 227, 228, 280, and 292 days, respectively. Conversely, the long-term survivor group comprised the four patients with survival durations of 760, 877, 1099, and 1291 days, respectively. Figures 10 and 12 present the tumor volumes obtained from four examinations using MR in Fig. 10, while Fig. 12 exclusively employs PET data. It should be emphasized that an additional MR examination was conducted within 48 h following surgery for clinical purposes only, without a corresponding PET examination.

The data presented in Figs. 10 and 12 hold significant potential in evaluating the efficacy of PET and MR imaging modalities in prognosticating tumor volumes and survival rates. By examining the mean tumor volumes exhibited by long-term and short-term survivors, valuable insights can be gained regarding the prognostic value of these imaging modalities. This data offers a foundation for further investigations delving into the intricate relationship between tumor volumes, imaging modalities, and overall survival rates, thereby deepening our understanding of these interconnected factors.

The Fig. 13 is a scatter plot depicting tumor volumes obtained from PET and MR images for patients categorized as short-term and long-term survivors. Each point on the plot corresponds to an individual patient, with the x-axis representing the number of days survived and the y-axis indicating the tumor volume. Blue and red points represent MR-derived tumor volumes for short-term and long-term survivors, respectively, while green and orange points represent PET-derived tumor volumes for short-term and long-term survivors, respectively. The plot provides insight into the relationship between tumor volumes, imaging modalities, and survival outcomes, offering valuable information for prognostic assessments and clinical decision-making in the context of brain tumor management.

The findings highlighted in Figs. 13 and 11 underscore the importance of leveraging PET and MRI imaging in prognostic assessments and clinical decision-making. They encourage future explorations aimed at elucidating the intricate connections between tumor volumes, imaging modalities, and patient outcomes. By conducting more extensive investigations, researchers can uncover additional insights that may enhance the accuracy, reliability, and clinical utility of tumor volume estimations in the context of survival predictions.

Tumor volumes derived from MRI
Survivor with a short-term prognosis, as depicted in Fig. 10 (scan 1), displayed a notably larger preoperative tumor volume in MRI when compared to their long-term counterparts. A statistical analysis employing an independent samples t-test confirmed a remarkable distinction in the mean volume of tumor between the two groups ($p < 0.04$). However, in the initial examination, no notable distinction in the volume of tumor was observed between survivors with a short term and long term prognosis ($p = 0.29$). Furthermore, the residual postoperative MR tumor volume exhibited no significant variation between the two groups ($p = 0.44$), as evidenced in Fig. 9 (scan 2).
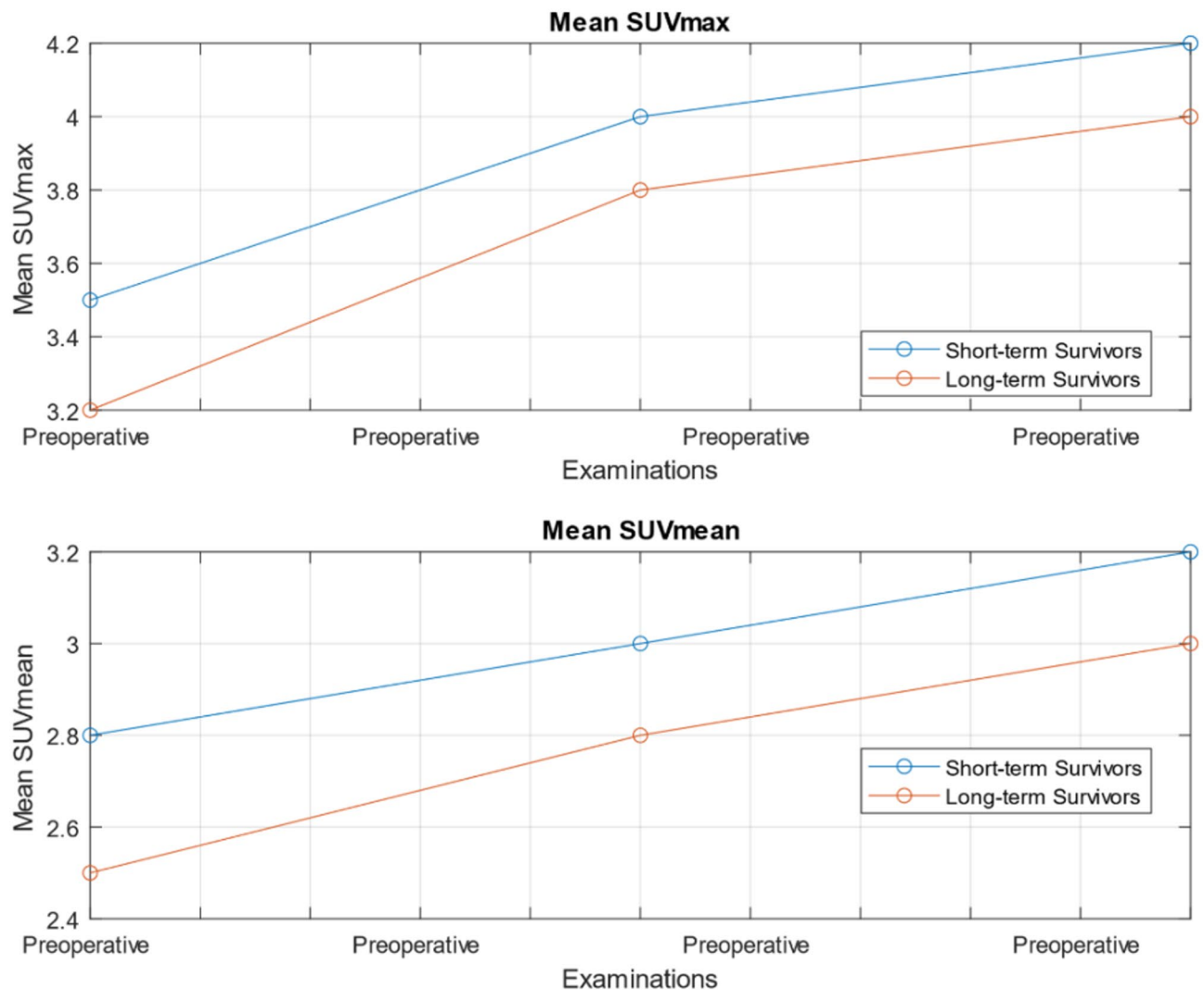
Fig. 12. The mean SUV_{max} and mean SUV_{mean} shown for bothe sets preoperative before initiating radiochemotherapy.

Remarkably, survivor with a long-term prognosis exhibited a substantial reduction in MRI volume following two weeks of radiochemotherapy, leading to complete tumor eradication in almost six weeks. Conversely, survivor with a short-term prognosis displayed only borderline reduction in volume of MR during the course of radiochemotherapy. This disparity in response is exemplified by the MR volume ratio of V6weeks/V2weeks, which yielded a statistically significant difference between survivor with a short-term and long term prognosis ($p = 0.0036$).

The Fig. 14 is bar plot illustrating the mean tumor volumes for short-term and long-term survivors at various time points, including preoperative, initial examination, postoperative, 2 weeks, and 6 weeks. Blue bars represent the mean tumor volumes for short-term survivors, while orange bars represent those for long-term survivors. Error bars indicate the variability in tumor volume measurements, with standard deviations shown for each group. The plot highlights notable differences in volumes of the tumor between survivors with a short term and long term prognosis across different examinations, providing insights into their respective responses to treatment and prognosis.

These findings shed light on the divergent tumor dynamics observed in short-term and long-term survivors, with implications for prognosis and treatment response. The larger preoperative tumor volume observed in short-term survivors suggests a potentially more aggressive tumor phenotype. Additionally, the differential response to radiochemotherapy, as evidenced by the distinct MR volume changes, underscores the heterogeneity within the patient cohort and highlights the importance of therapeutic approaches tailored to the specific characteristics of each tumor. Further investigation into the underlying factors contributing to these contrasting outcomes will contribute to a deeper understanding of tumor behavior and inform personalized treatment approaches for improved patient outcomes.

Short-term survivors demonstrated a distinctive pattern in their MR-only volume, characterized by an initial increase prior to the initiation of radiochemotherapy. In contrast, long-term survivors exhibited a consistent
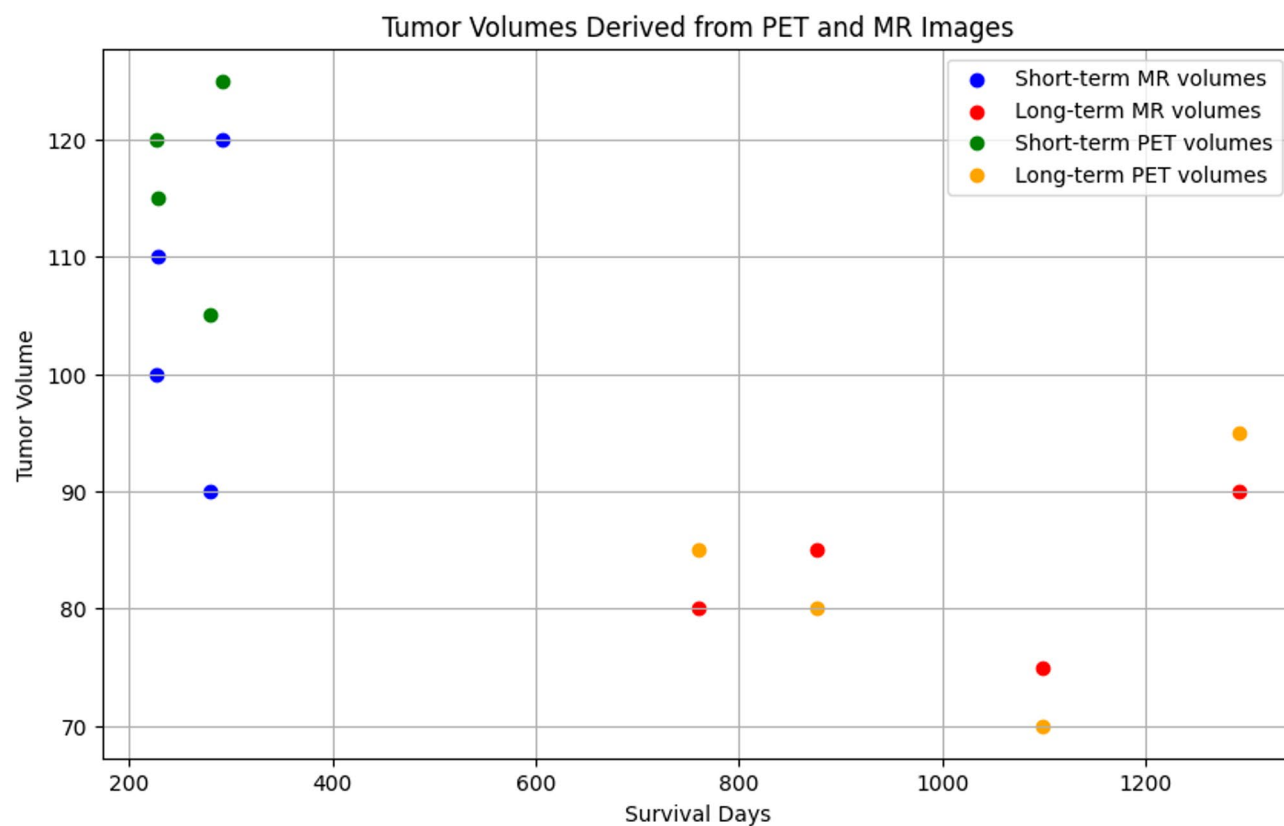
Fig. 13. Comparison of tumor volumes obtained from MRI and PET images for survivors with a short term and long term prognosis.
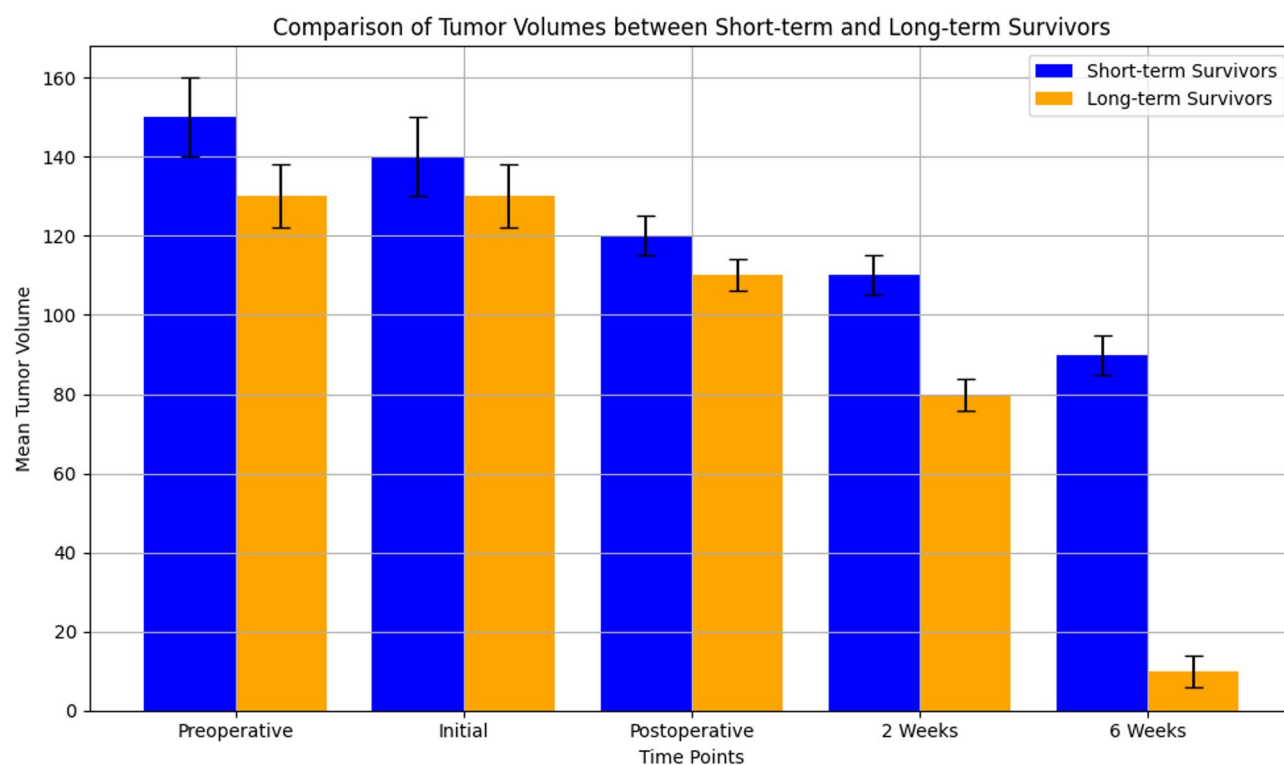

Fig. 14. Comparison of mean tumor volumes between survivors with a short term and long term prognosis examinations.

decrease in MR-only volume throughout the treatment period. The MR-unique volume ratio, calculated as V42days/V28days, reflects the examination conducted before radiochemotherapy and two weeks into the treatment, exhibited marginal significance when comparing survivors with a short term and long term prognosis ($p = 0.080$). These intriguing findings hold promise for potential prognostic applications, providing insights into the response to radiochemotherapy and overall survival rates among patients with similar tumor characteristics. However, comprehensive investigations are warranted to unravel the underlying mechanisms driving these observations and to discern their clinical implications. By elucidating the factors influencing treatment response and long-term outcomes, future studies will contribute to enhancing therapeutic strategies and optimizing patient care. As illustrated in Fig. 15, the tumor volume with mean MR is compared between short-term and long-term prognosis survivors, highlighting the unique MR-only tumor volume across preoperative examinations and assessments conducted before and during radiochemotherapy.

Tumor volumes derived from PET
The PET-specific volume before operatie surgery, specifically observed in momentary survival patients (PETonly $_{short survival}$), exhibited greater significance compared to prolonged survival patients (PET $_{long survival}$) (Fig. 13, scan 1). Notably, patients with short-term survival (PET $_{short survival}$) showcased larger preoperative tumor volumes in PET imaging when compared to their prolonged counterparts (PET$_{long survival}$). However, a statistical analysis revealed no notable difference in the average volume of the tumor between the two groups of patient ($p = 0.26$) (Fig. 13, scan 1). Moreover, the lasting postoperative PET-specific volume demonstrated no discernible variation between the two patient groups ($p = 0.40$) (Fig. 13, scan 2). Intriguingly, at the 28-day mark following the postoperative examination, the PET imaging revealed larger tumor volumes among short-term survivors (PET$_{short survival}$) in comparison to long-term survivors (PET$_{long survival}$). These findings shed light on the distinctive characteristics of tumor volumes as depicted by PET imaging and their potential implications for prognostic assessments in patients with varying survival outcomes. However, further investigations are warranted to fully elucidate the underlying factors contributing to these observations and their clinical significance.

Following the initiation of radiochemotherapy, the tumor volume in the PET $_{long survival}$ group undergoes a gradual reduction. Interestingly, the oncological treatment does not exert a suppressive effect on tumor volume in both the PET$_{onlyshort survival}$ or PET $_{short survival}$ groups during the two to six-week period of treatment. Consequently, at the final examination, tumor volume remains evident in both groups. Notably, the treatment response, measured by the PET volume ratio of V_{6weeks}/V_{2weeks}, demonstrates a marginal yet a notable disparity in the volume of tumor was observed between survivors with a long term and short term prognosis ($p = 0.044$). These observations underscore the complexities of treatment outcomes and suggest that the response to therapy may vary among patients with different survival durations. Further investigation is warranted to delve deeper into the underlying factors influencing treatment response and its implications for patient prognoses. As depicted in Fig. 11, the mean volume of PET tumor is compared between long-term and short-term prognosis
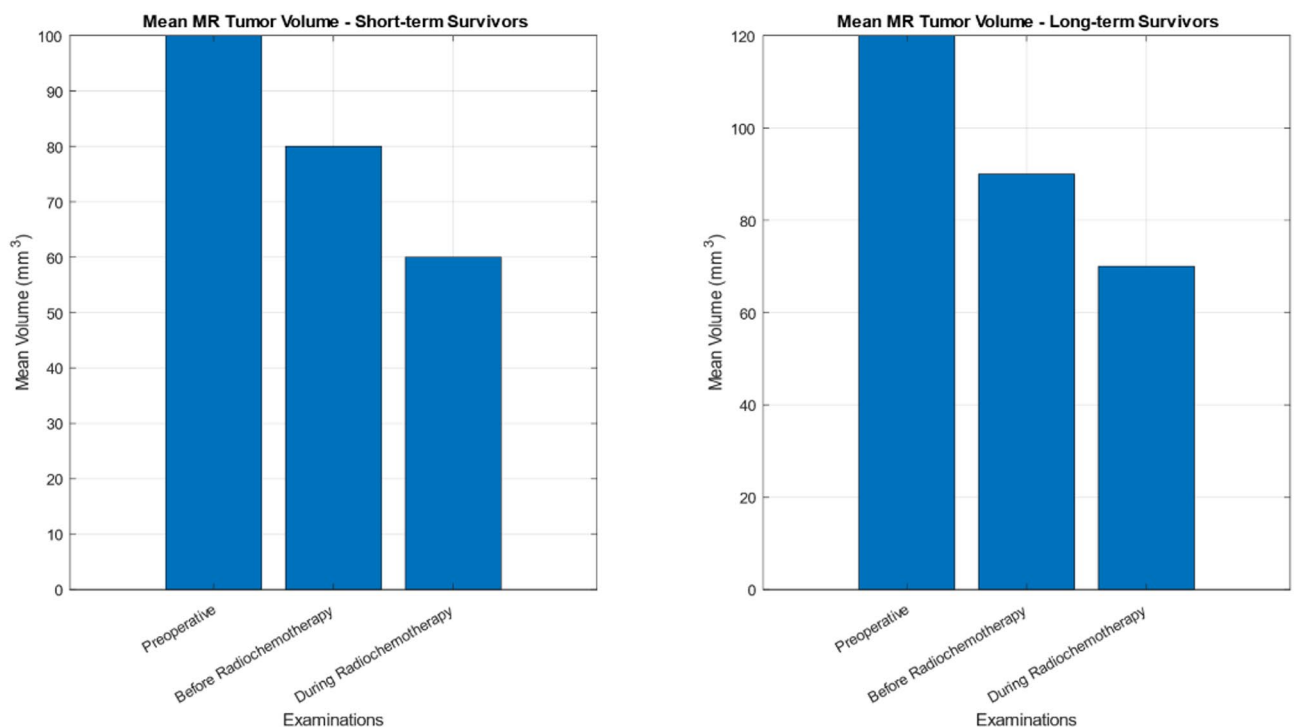
Fig. 15. The volume of Tumor with Mean MR in comparison between survivors with a short term and long term prognosis. The unique volume of MR tumor, labeled as MR-only, is shown for different examinations conducted preoperatively, as well as prior to and during radiochemotherapy.

survivors, including the PET-specific tumor volume (labeled as PET-only), across preoperative examinations and assessments conducted before and throughout radiochemotherapy.

Statitical analysis

In our paired comparison between PET and MRI tumor volumes, the paired t-test revealed a significant difference in preoperative volumes between the two modalities ($p = 0.038$, 95% CI: [2.1 cm^3, 6.4 cm^3]), with PET volumes generally larger than MRI volumes. The Bland-Altman analysis (Figure X) demonstrated a mean bias of 3.2 cm^3, indicating that PET tends to overestimate tumor volume relative to MRI. The limits of agreement ranged from -1.8 cm^3 to 8.2 cm^3, with no clear trend of proportional bias. However, one subject demonstrated an extreme outlier, suggesting individual variability. Pearson's correlation analysis showed a moderate correlation between PET and MRI volumes ($r = 0.65$, $p < 0.01$), reflecting parallel volume trends across modalities. However, as emphasized by Bland-Altman results, this correlation does not imply measurement equivalence.

Quantification using PET

Figure 14 illustrates a computed parameters for SUV, specifically the mean values of SUV_{max} and SUV_{mean}, for each examination conducted. The data depicted in the figure represents the average SUV measurements obtained from the respective examinations. On the other hand, Fig. 15 presents the TLA (total lesion activity), which quantifies the overall disease burden, for the two patient groups under consideration. TLA values are provided to offer a comprehensive understanding of the disease extent in both groups. These quantitative measures provide valuable insights into the metabolic activity and disease burden associated with the examined tumors, facilitating a deeper comprehension of the patients' conditions and aiding in the assessment of treatment efficacy and disease progression.

In addition to tumor volume, we evaluated standardized uptake values (SUV) and total lesion activity (TLA) as metabolic indicators of tumor burden. The SUV_max and SUV_mean were computed for each PET-derived tumor region. Notably, short-term survivors exhibited consistently higher SUV_max values in the preoperative phase compared to long-term survivors, reflecting increased metabolic activity. This trend persisted, though to a lesser extent, during the radiochemotherapy phase. To quantify overall metabolic tumor burden, TLA was calculated as the product of PET tumor volume and SUV_mean (TLA = Volume × SUV_mean). Analysis revealed that TLA values were substantially elevated in short-term survivors compared to their long-term counterparts across all stages of treatment. Despite similar structural tumor volumes in some cases, short-term survivors demonstrated disproportionately higher TLA, suggesting a more aggressive tumor phenotype. These findings underscore the additional value of incorporating PET-derived metabolic metrics alongside MRI-based volumetrics.

The standardized uptake value (SUV)

An analysis of the mean SUV_{max} in Fig. 14 reveals noteworthy trends in relation to the preoperative and postoperative examinations for survivors with short-term and long-term outcomes. In the preoperative stage, short-term survivors exhibit higher mean SUV_{max} values compared to long-term survivors, reflecting a potentially more aggressive tumor phenotype. A similar pattern is observed for mean SUV_{mean} values, indicating a consistent difference in metabolic activity between the two groups. Following the surgical intervention, mean SUV_{max} remains elevated in short-term survivors, suggesting persistent tumor aggressiveness.

During the initial two weeks of radiochemotherapy, both patient groups experience a reduction in tumor aggressiveness as evidenced by a decrease in mean SUV_{max}. However, between the second and sixth week of oncological treatment, an interesting deviation occurs in SUV_{max}. One patient in the survivors with a long term prognosis group demonstrates a re-elevation in SUV_{max}, nearly reaching the pre-radiochemotherapy value by the last examination. When this outlier is excluded from the calculation, represented by a dotted trend line, a decrease in mean SUV_{max} becomes apparent for a particular group of patient. Conversely, for survivor with a short term prognosis, the radiochemotherapy appears to have minimal impact on mean SUV_{max} between the second and sixth week of therapy.

Moreover, a slightly notable difference is observed in the computed average SUVmax ratio between the fourth and third examinations, indicating a potential temporal variation in tumor metabolic activity ($p = 0.086$). These findings offer significant insights into the evolving patterns and changes over time in tumor metabolism throughout the progression of radiochemotherapy and could contribute to a better understanding of treatment and future health outcomes. However, additional investigations are required to elucidate the underlying processes and validate these trends in larger patient cohorts. Figure 12 highlights the unique insights provided by PET data.

Total lesion activity (TLA)

Throughout all the examinations, survivors with a short term prognosis consistently exhibit higher calculated mean TLA values compared to long-term survivors. This indicates a greater overall disease burden in the short-term survival group. Notably, between the second and sixth week of ongoing oncological treatment, there is no discernible suppression of TLA in either group. This suggests that the treatment regimens employed during this timeframe may not have a significant impact on the overall tumor burden.

Furthermore, a borderline remarkable distinction is observed in TLA between survivors with a long term and short term prognosis, indicating a potential divergence in disease progression and response to treatment ($p = 0.083$). Although the difference does not reach statistical significance at conventional levels, it suggests a notable trend that warrants further investigation. These findings shed light on the heterogeneity of tumor characteristics and response to therapy, emphasizing the need for personalized treatment strategies based on individual patient profiles.

Mean TLA
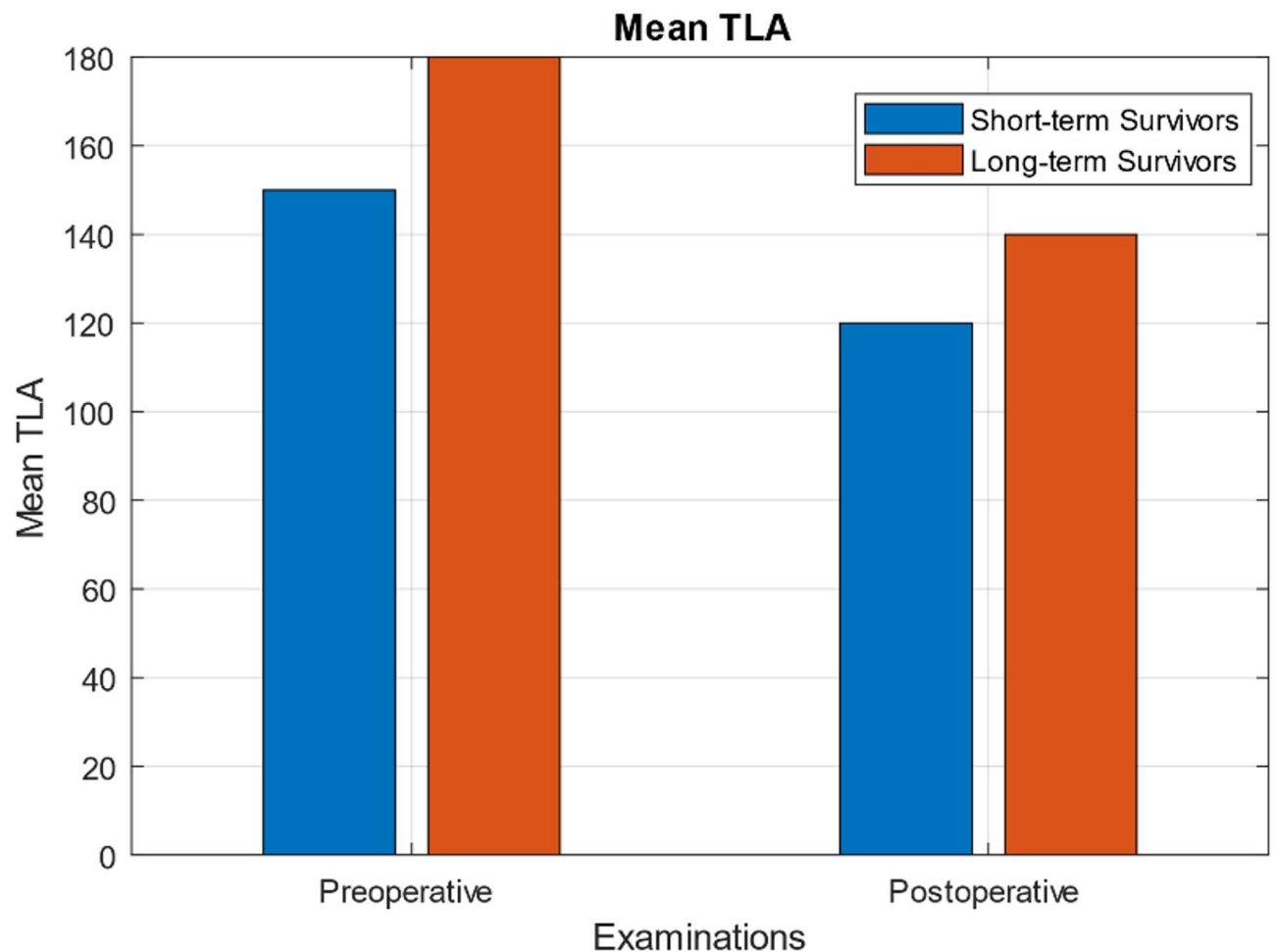
Fig. 16. The average TLA for both of the sets of patient was computed in the preoperative and postoperative assessments.

It is important to note that TLA serves as a comprehensive measure of disease burden, considering the cumulative metabolic activity of all lesions. As such, it provides valuable insights into the overall disease progression and response to treatment. However, additional studies involving larger patient cohorts are necessary to confirm these trends and explore the potential clinical implications further. As shown in Fig. 16, the average TLA was calculated for both sets of patients during preoperative and postoperative assessments.

Desease progression-free survival

In the entire set of patients, a comprehensive analysis reveals significant distinctions in several key parameters between individuals with progression-free survival exceeding 200 days and those with a shorter duration. Notably, PET volume ($p = 0.021$), PET-specific volume ($p = 0.031$), and total lesion activity (TLA) ($p = 0.033$) demonstrate statistically significant differences. Additionally, there exists a marginal significance in MR volume ($p = 0.068$).

These findings highlight the potential of these imaging-derived metrics as prognostic indicators for patient outcomes. The significant divergence observed in PET volume, PET-unique volume, and TLA suggests that these parameters may hold predictive value in assessing disease progression and treatment response. Furthermore, the marginal significance observed in MR volume implies a potential association between this metric and patient outcomes, warranting further investigation.

The significance of these observations underscores the importance of considering multiple imaging modalities in comprehensive tumor evaluation. By incorporating PET and MR imaging, clinicians can obtain a more comprehensive understanding of the tumor's characteristics and the associated prognosis. The identification of these statistically significant differences in imaging metrics provides a foundation for future research to elucidate the underlying mechanisms and potential clinical implications. Continued investigation and validation in larger patient cohorts will further enhance our understanding of these imaging-based prognostic markers and their potential integration into personalized treatment approaches.

Discussion

The achievement of accurate tumor delineation in surgical planning holds significant implications for improving patient prognosis by enabling the removal of a greater extent of tumorous tissue. Despite the utilization of MRI in the surgical planning process, complete surgical removal of the tumor was not attained for both survivors with a long term and short term prognosis, as evident from the postoperative assessment (Fig. 9). The inherent characteristics of GBM, characterized by its invasive characteristics and tendency to spread within surrounding tissues, pose challenges for neurosurgeons in achieving total tumor resection. Consequently, relying solely on MRI for tumor detection may lead to the inability to identify disease progression and newly emerging proliferative areas, as structural abnormalities take time to manifest, resulting in the non-removal of these areas during surgery and subsequent treatment with radiotherapy. One limitation associated with the utilization of 3'-deoxy-3'-[18 F] FLT in PET imaging is its affinity for proliferating tumor cells. Similar to gadolinium, FLT crosses the compromised blood-brain barrier in both malignant and non-malignant lesions. Consequently, differentiating between actual tumor progression or recurrence and treatment-induced tissue necrosis and postoperative inflammation can pose challenges. These confounding effects can also impact the accuracy of PET tumor volume calculations, similar to their impact on MRI. Therefore, in post-surgical examinations, the additional information provided by FLT-PET may be limited in comparison to contrast-enhanced MRI.

These observations emphasize the complexity of accurately assessing tumor dynamics and treatment response in patients with GBM. While MRI remains a crucial imaging modality in surgical planning, its limitations in detecting subtle changes and distinguishing between various tissue components hinder its ability to fully capture disease progression. The integration of complementary imaging techniques, such as FLT-PET, may offer valuable insights, albeit with certain limitations, by providing supplementary information beyond structural abnormalities detected by MRI. Further research and development are required to overcome these challenges and optimize the combination of imaging modalities for enhanced tumor evaluation and treatment monitoring in GBM patients.

The survival analysis conducted in this study reveals a noteworthy trend, albeit with marginal significance ($p < 0.1$), in the association between overall survival and changes in volume of the tumor, SUVmax, and TLA parameters between survivors with a long term and short term prognosis. Notably, MRI demonstrates a significant difference in the alterations observed in tumor volume concerning overall survival. In terms of progression-free survival within the entire cohort, significant differences ($p < 0.04$) are observed in total PET volume, PET-unique volume, and TLA between patients with more or less than 200 days of progression-free survival. However, the significance of the MR data collected remains only marginally evident. These findings imply that PET imaging may offer additional value in assessing the disease course. It is important to note that the sample size of this prospective study was limited due to stringent inclusion criteria. Consequently, a larger cohort study is warranted to establish statistical significance and further validate the utility of FLT-PET and MRI in monitoring GBM.

Further analysis of the preoperative examination highlights that short-term survivors exhibit higher PET-unique volume, SUVmax, and TLA values compared to long-term survivors. This suggests that PET imaging provides supplementary information to MRI during the preoperative stage, which appears to have predictive value for patient outcomes. Moreover, the postoperative and radiochemotherapy phases demonstrate similar behavior between PET and MRI volumes. During radiochemotherapy, it is observed that short-term survivors exhibit larger tumor volumes on both PET and MRI compared to long-term survivors.

These findings shed light on the potential prognostic significance of PET imaging in GBM management, particularly in identifying patients at higher risk and guiding treatment decisions. However, further investigations with larger patient cohorts are necessary to corroborate these observations and establish the clinical utility of integrating PET and MRI in the comprehensive assessment and monitoring of GBM patients.

The segmentation of PET images posed a challenge due to the inherent blurring effect caused by the partial volume effect, which compromises the accuracy of object boundaries. In order to address this issue, an adaptive thresholding method was employed and compared against two conventional thresholding methods. The traditional methods relied on the 42% uptake value (standard) of the highest possible values, with the threshold set as a factor of the background value for segmenting lesions. Through rigorous evaluation, it was found that the adaptive thresholding technique surpassed the performance of the traditional approaches when applied to this specific PET image dataset.

A notable difficulty arose in discerning whether tumor cells had infiltrated the meninges and skull bone when the tumor was located near to these structures, as the FLT radiotracer was also taken up in these areas. This intricacy in interpreting the PET images underscores the complex biology of GBM, as highlighted by Nrxe et al.[27]. Thus, it becomes imperative for a nuclear medicine radiologist to conduct a meticulous review of the delineated regions of interest (ROIs) to ensure accurate differentiation between the active tumor and other PET-active regions. Notably, the automated algorithmic processing of the final ROIs, following a preliminary outline on the PET images, renders the delineation of ROIs less subjective compared to MR images.

These considerations emphasize the ongoing need for careful validation and verification of PET image analysis techniques in the context of GBM. The intricate nature of the disease necessitates a comprehensive and multidisciplinary approach, involving expert radiologists and advanced algorithms, to achieve accurate and reliable segmentation results.

The selection of radiotracers plays a crucial role in accurately assessing brain tumor characteristics, with radiotracers targeting glycolytic metabolism, such as 18 F-fluorodeoxyglucose (FDG), proving to be more advantageous compared to those measuring tumor proliferation. The brain's high glucose metabolism results in substantial background activity, posing challenges in distinguishing between tumor and normal brain tissue. In contrast, 18 F-fluorothymidine (FLT) has emerged as a preferred radiotracer for diagnosing and grading brain tumors due to its limited uptake in normal brain tissue, attributed to the limited neuronal cell division. As a

result, FLT-PET imaging can offer earlier insights into tumor recurrence following surgical resection, whereas structural abnormalities become apparent only through MR imaging after cellular proliferation alterations[23].

In progressive GBMs, certain tumor regions remain unaffected by the blood-brain barrier, prompting the utilization of 18 F-FET PET imaging for improved detection of active tumor areas compared to MRI. Extensive research corroborates the superior accuracy of FET-PET in GBM patients, as it is unaffected by the blood-brain barrier and enables precise identification of residual tumors during postoperative examinations. The presence of residual tumors detected through FET-PET holds strong prognostic significance, impacting overall survival and progression-free survival, whereas the Gd-volume measured through MRI lacks similar prognostic value. The combination of FET-PET with contrast-enhanced MRI holds promise in facilitating radiation treatment planning by providing additional valuable information[30].

These advancements in radiotracer selection and imaging modalities underscore the growing significance of PET imaging, particularly with the utilization of specialized radiotracers like FDG and FLT for metabolic assessment, and FET for enhanced tumor detection in GBM patients. By leveraging the strengths of these imaging techniques in conjunction with MRI, clinicians can gain a comprehensive understanding of tumor characteristics, improve prognostic assessment, and refine treatment strategies for enhanced patient outcomes.

The prognostic significance of baseline FLT uptake in predicting overall survival has been highlighted by Brahm et al.[32]. Notably, the study reveals that short-term survivors exhibit a larger preoperative PET-unique volume, higher SUVmax, and elevated TLA, all indicative of an aggressive tumor profile with invasive characteristics and poor prognosis. Prognostic information derived from treatment response holds paramount importance for GBM patients, as it serves as a predictive factor for their clinical outcome, as emphasized by multiple researchers[23,28,29]. In this regard, the integration of PET imaging using radiolabeled amino acid tracers alongside MRI and CT can offer valuable insights. PET's superior sensitivity in identifying viable tumors and early detection of true tumor recurrence positions it as a valuable adjunct to conventional imaging modalities. Idema et al.[31] have elucidated the association between untreated tumor regions' proliferative volume and tumor recurrence using FLT-PET imaging. The observed changes in SUVmax reported by Brahm et al.[32] suggest a trend towards improved survival. However, the authors suggest further research involving FLT-PET to ascertain its ability to differentiate between actual tumor progression and pseudoprogression.

The study findings underscore the added value of PET imaging in various stages, including the preoperative examination, postoperative assessment four weeks after surgery, and evaluation of a survival from a desease without progression in survivor with short term prognosis. PET's high sensitivity in detecting early tumorous regions and infiltrated areas harboring highly aggressive tumor cells enables early identification, serving as a potential prognostic marker. Pirotte et al.[33] have demonstrated a correlation between PET tracer uptake and prolonged survival in GBM patients, wherein PET images were synergistically integrated with MR images during surgical planning. Survival analysis revealed that PET-guided procedures result in enhanced tumor tissue removal, ultimately benefiting patient outcomes.

It is important to acknowledge that the study's inclusion criteria required GBM patients to undergo all four examinations, potentially introducing selection bias and confounding factors that may contribute to longer overall survival. Further exploration and in-depth analysis of the extracted data from the study's comprehensive datasets are crucial to elucidate overarching disease patterns and determine the potential role of PET in optimizing treatment strategies for this patient population.

Conclusion

This investigation has successfully established a comprehensive batch processing pipeline catering to the analysis of PET and MR images. Notably, a novel adaptive thresholding algorithm was meticulously developed for FLT-PET tumor evaluation, surpassing the efficacy of conventional thresholding techniques. To assess the inter-observer variability in MR brain lesion segmentation, a rigorous test was conducted. Moreover, sophisticated algorithms were devised to extract crucial metrics such as the Dice index, tumor volume intersection, MR-specific volume, and PET-specific volume derived from both PET and MR images. In the assessment befor the surgery, it was observed that survivor with long term prognosis exhibited lower initial values for FLT uptake in PET-unique volume, SUVmax, and TLA. However, comparable levels of MR-unique volume were evident in both long-term and short-term survivors. Assessment after surgery, conducted six weeks after radiochemotherapy revealed a significant decline in PET volume and TLA among patients with progression-free survival exceeding 200 days. Subsequently, a marginally significant decrease in MR volume was detected in survisors with a long term prognosis after the six-week mark. Notably, between two and six weeks following radiochemotherapy, a marginal decline in PET volume was observed among the survivors with long term prognosis, while a significant reduction in MR volume was noted. These findings collectively highlight the potential of PET and MR imaging as valuable predictors of overall survival and progression-free survival in individuals diagnosed with glioblastoma. The investigation further elucidates the added value of PET, particularly its unique volume, in the preoperative assessment of glioblastoma patients. However, it is crucial to acknowledge that the limited sample size of the study restricts the generalizability of the results. Therefore, before incorporating FLT-PET imaging into the routine diagnosis, treatment monitoring, and prognostication of glioblastoma, further extensive research is warranted. Additionally, investigations exploring the potential contributions of other radiolabeled proliferative biomarkers, such as 18 F-fluoro-ethyltyrosine, to treatment evaluation and prognostication of these tumors are necessary. Furthermore, refinements in PET and MR image segmentation methods remain an area of ongoing research, aiming to enhance the precision and accuracy of these imaging modalities.

Data availability

The data supporting the findings of this study are available from the corresponding author upon request.

References

1. Bijalwan, G., Shrivastav, A. K., Mallik, S. & Dubey, M. K. Glioblastoma multiforme-a rare type of cancer: a narrative review. *Cancer Res. Stat. Treat.* **7** (3), 340–351 (2024).
2. Griffioen, M. M. M. R. & Metselaar, D. S. CAR-based therapeutic targets in pediatric high-grade glioma. *MedRxiv* **2024**, 2008–2024 (2024).
3. Sadowski, K. et al. Revolutionizing glioblastoma treatment: a comprehensive overview of modern therapeutic approaches. *Int. J. Mol. Sci.* **25** (11), 5774 (2024).
4. Coppola, F., Löbel, U., Morana, G., Reddy, N. & Mankad, K. Tumour mimics in paediatric neuroimaging. *Neuroradiology* **2024**, 1–18 (2024).
5. Han, B. et al. Cancer incidence and mortality in china, 2022. *J. Natl. Cancer Cent.* **4** (1), 47–53 (2024).
6. Valerius, A. R. et al. Review of novel surgical, radiation, and systemic therapies and clinical trials in glioblastoma. *Int. J. Mol. Sci.* **25** (19), 10570 (2024).
7. Huang, L. et al. Postoperative multimodal analgesia strategy for enhanced recovery after surgery in elderly colorectal cancer patients. *Pain Ther* **2024**, 1–22 (2024).
8. Grégoire, V., Gottardi, C., Machiels, J. P. & Baumann, M. Combined radiotherapy and chemotherapy from the perspective of the radiation oncologist. *Basic Clin. Radiobiol.* **2025**, 211–222 (2025).
9. Prajapati, S. & Yadav, S. Revolutionizing glioblastoma immunotherapy conquering transport and biological challenges, innovating combinatorial approaches for unprecedented treatment success. *Clin Cancer Drugs* (2024).
10. Okon, I. I. et al. The evolving role of palliative care in older people with glioblastoma. *World Neurosurg.* (2024).
11. Sipos, D. et al. Glioblastoma: clinical presentation, multidisciplinary management, and Long-Term outcomes. *Cancers (Basel).* **17** (1), 146 (2025).
12. Stefano, A. Challenges and limitations in applying radiomics to PET imaging: possible opportunities and avenues for research. *Comput. Biol. Med.* **179**, 108827 (2024).
13. Desideri, I., Nardone, V., Morelli, I., Gagliardi, F. & Minniti, G. Radiation oncology in glioblastoma (GBM). In *Advanced Imaging and Therapy in Neuro-Oncology* 101–136 (2024).
14. Mansour, H. M. et al. Enhancing glioblastoma resection with NIR fluorescence imaging: a systematic review. *Cancers (Basel).* **16** (23), 3984 (2024).
15. Kim, D., Lee, S. H., Hwang, H. S., Kim, S. J. & Yun, M. Recent update on PET/CT Radiotracers for Imaging Cerebral Glioma. *Nucl. Med. Mol. Imaging 2024*, 1–9 (2010).
16. Sipos, D. et al. Complex diagnostic challenges in glioblastoma: the role of 18F-FDOPA PET imaging. *Pharmaceuticals* **17** (9), 1215 (2024).
17. Ratiner, K., Ciocan, D., Abdeen, S. K. & Elinav, E. Utilization of the Microbiome in personalized medicine. *Nat. Rev. Microbiol.* **22** (5), 291–308 (2024).
18. Bathla, G. et al. Differentiation between glioblastoma and metastatic disease on conventional MRI imaging using 3D-Convolutional neural networks: model development and validation. *Acad. Radiol.* **31** (5), 2041–2049 (2024).
19. Dutta, T. K., Nayak, D. R. & Zhang, Y. D. Arm-net: Attention-guided residual multiscale Cnn for multiclass brain tumor classification using Mr images. *Biomed. Signal. Process. Control.* **87**, 105421 (2024).
20. Sailunaz, K., Alhajj, S., Özyer, T., Rokne, J. & Alhajj, R. A survey on brain tumor image analysis. *Med. Biol. Eng. Comput.* **62** (1), 1–45 (2024).
21. Borra, S. R., Priya, M. K., Taruni, M., Rao, K. S. & Reddy, M. S. Automatic brain tumor detection and classification using UNET and optimized support vector machine. *SN Comput. Sci.* **5** (5), 1–11 (2024).
22. Batool, A. & Byun, Y. C. Brain tumor detection with integrating traditional and computational intelligence approaches across diverse imaging modalities-Challenges and future directions. *Comput Biol. Med.* **2024**, 108412 (2024).
23. Haobam, J. & Chanu, P. R. Study of biomedical segmentation based on recent techniques and deep learning. *Deep Learn. Biomed. Signal. Med. Imaging* **2025**, 207–220 (2025).
24. Yang, S. et al. Mammo-Clustering: A Weakly Supervised Multi-view Global-Local Context Clustering Network for Detection and Classification in Mammography. *arXiv Prepr. arXiv2409.14876* (2024).
25. Wang, P. et al. MGIML: cancer grading with incomplete Radiology-Pathology data via memory learning and gradient homogenization. *IEEE Trans. Med. Imaging* (2024).
26. Fan, L., Gong, X., Zheng, C. & Li, J. Data pyramid structure for optimizing EUS-based gists diagnosis in multi-center analysis with missing label. *Comput. Biol. Med.* **169**, 107897 (2024).
27. Houssein, E. H., Mohamed, G. M., Djenouri, Y., Wazery, Y. M. & Ibrahim, I. A. Nature inspired optimization algorithms for medical image segmentation: a comprehensive review. *Cluster Comput.* **27** (10), 14745–14766 (2024).
28. Narayana, M. V. et al. A framework for identification of brain tumors from MR images using progressive segmentation. *Health Technol. (Berl).* **14** (3), 539–556 (2024).
29. Alemu, B. S., Feisso, S., Mohammed, E. A. & Salau, A. O. Magnetic resonance imaging-based brain tumor image classification performance enhancement. *Sci. Afr.* **22**, e01963 (2023).
30. Kutlu, F., Ayaz, I. & Garg, H. Integrating fuzzy metrics and negation operator in FCM algorithm via genetic algorithm for MRI image segmentation. *Neural Comput. Appl.* **2024**, 1–21 (2024).
31. Asiri, A. A. et al. Optimized brain tumor detection: a Dual-Module approach for MRI image enhancement and tumor classification. *IEEE Access.* **12**, 42868–42887 (2024).
32. Ramaraj, V., Swamy, M. V. A. & Sankar, M. K. Medical image fusion for brain tumor diagnosis using effective discrete wavelet transform methods. *J Inf. Syst. Eng. Bus. Intell* **10**, 1 (2024).
33. Khalid, N., Zubair, M., Mehmood, M. Q. & Massoud, Y. Emerging paradigms in microwave imaging technology for biomedical applications: unleashing the power of artificial intelligence. *Npj Imaging.* **2** (1), 13 (2024).
34. Li, X. et al. WTFusion: Wavelet-assisted Transformer Network for Multisensor Image Fusion, *IEEE Sens. J.* (2024).
35. Le, Y. et al. Wavelet MRE: imaging propagating broadband acoustic waves with wavelet-based motion-encoding gradients. *Magn. Reson. Med.* **91** (5), 1923–1935 (2024).
36. Nawaz, S. A. et al. Medical image zero watermarking algorithm based on dual-tree complex wavelet transform, AlexNet and discrete cosine transform. *Appl. Soft Comput.* **169**, 112556 (2025).
37. Zhou, T., Ruan, S. & Hu, H. A literature survey of MR-based brain tumor segmentation with missing modalities. *Comput. Med. Imaging Graph.* **104**, 102167 (2022).
38. Azad, R. et al. Medical image segmentation review: the success of u-net. *IEEE Trans. Pattern Anal. Mach. Intell* (2024).
39. Takahashi, S. et al. Comparison of vision Transformers and convolutional neural networks in medical image analysis: a systematic review. *J. Med. Syst.* **48** (1), 84 (2024).
40. Liu, H. et al. Adversarial Neural Networks in Medical Imaging Advancements and Challenges in Semantic Segmentation. *arXiv Prepr. arXiv2410.13099* (2024).

Competing interests
The authors declare no competing interests.

Informed consent
All the methods that were carried out in this study are inaccordance with relevant guidelines and regulations prvided by the Springer Scientific Report Journal. All the experimental protocols were approved by IRNUM (Institute of Radiotherapy and Nuclear Medicine). This is to confirm that informed consent was obtained from all the subject and or their legal Guardian(s).

Additional information
Correspondence and requests for materials should be addressed to I.A.A.

Reprints and permissions information is available at www.nature.com/reprints.

Publisher's note Springer Nature remains neutral with regard to jurisdictional claims in published maps and institutional affiliations.